

# Plasma membrane remodeling determines adipocyte expansion and mechanical adaptability

---

Received: 2 June 2022

---

Accepted: 5 November 2024















---

Published online: 28 November 2024

---

 Check for updates

---

María C. M. Aboy-Pardal <sup>1</sup>, Marta C. Guadamillas <sup>1,9</sup>, Carlos R. Guerrero<sup>2</sup>, Mauro Català-Montoro<sup>1,15</sup>, Mónica Toledano-Donado <sup>1,15</sup>, Sara Terrés-Domínguez<sup>1,15</sup>, Dácil M. Pavón<sup>1,10,15</sup>, Víctor Jiménez-Jiménez <sup>1,11</sup>, Daniel Jimenez-Carretero <sup>3</sup>, Moreno Zamai <sup>4</sup>, Cintia Folgueira <sup>5,12</sup>, Ana Cerezo<sup>1,13</sup>, Fidel-Nicolás Lolo <sup>1</sup>, Rubén Nogueiras <sup>5</sup>, Guadalupe Sabio<sup>6,14</sup>, Miguel Sánchez-Álvarez <sup>1,7</sup>, Asier Echarri <sup>1,8</sup>, Ricardo Garcia <sup>2</sup> & Miguel A. Del Pozo <sup>1</sup> 

---

Adipocytes expand massively to accommodate excess energy stores and protect the organism from lipotoxicity. Adipose tissue expandability is at the center of disorders such as obesity and lipodystrophy; however, little is known about the relevance of adipocyte biomechanics on the etiology of these conditions. Here, we show in male mice in vivo that the adipocyte plasma membrane undergoes caveolar domain reorganization upon lipid droplet expansion. As the lipid droplet grows, caveolae disassemble to release their membrane reservoir and increase cell surface area, and transfer specific caveolar components to the LD surface. Adipose tissue null for caveolae is stiffer, shows compromised deformability, and is prone to rupture under mechanical compression. Mechanistically, phosphoacceptor Cav1 Tyr14 is required for caveolae disassembly: adipocytes bearing a Tyr14Phe mutation at this residue are stiffer and smaller, leading to decreased adiposity in vivo; exhibit deficient transfer of Cav1 and EHD2 to the LD surface, and show distinct Cav1 molecular dynamics and tension adaptation. These results indicate that Cav1 phosphoregulation modulates caveolar dynamics as a relevant component of the homeostatic mechanoadaptation of the differentiated adipocyte.

Healthy white adipose tissue (WAT) safely stores energy in lipid droplets (LDs), gathering excess lipids from the bloodstream, and protecting peripheral organs (liver, pancreas, vascular wall) from ectopic fat deposition and lipotoxicity<sup>1–5</sup>. To store fat, adipocytes considerably fluctuate their volume depending on the balance between nutrient intake and organism energy demands<sup>6</sup>, an ability commonly referred to as *expandability*. Adipose tissue expandability is severely impaired in lipodystrophy, a condition where fat depots are partially or totally depleted<sup>7–11</sup>. Common metabolic disorders resulting from adipose tissue insufficiency involve

dyslipidemia, hepatic steatosis and impaired glucose metabolism<sup>12</sup>. These alterations resemble the main comorbidities of obesity, characterized by an exhaustion of the physiological capacity of adipose tissue due to chronic energy surplus<sup>13,14</sup>. Unraveling the mechanisms behind adipose tissue expandability is essential to understand the physiopathology of both conditions.

Adipose tissue expandability is partly defined by physical constraints from its environment: elimination of the main collagen component of adipose tissue (collagen IV) favors increased adipocyte size and improved metabolic profile in genetic models of

obesity<sup>15</sup>. However, intrinsic mechanical adaptation capability of the adipocyte is also at play. Cell expansion poses a challenge to the integrity of the plasma membrane (PM), and mechanisms ensuring membrane plasticity are needed. This is paramount because the mechanical rupture of adipocytes could shed to their surrounding environment large quantities of potentially cytotoxic materials, triggering a damaging inflammation process. However, little is known about the molecular and cellular mechanisms that protect adipocytes from the mechanical stress induced by massive fat accumulation.

Caveolae are PM, flask-shaped nanoinvasions of 60–90 nm in diameter<sup>16,17</sup>, with a specific lipid and protein composition<sup>18–21</sup> particularly abundant in adipocytes. Initially linked to endocytosis regulation<sup>22</sup> and organization of cell signaling<sup>23–27</sup>, these structures also function as mechanosensing and mechanotransduction devices that flatten when PM tension is increased<sup>28–33</sup>. On the contrary, conditions that reduce tension in the cell favor caveolae organization into higher-order clustered structures (named rosettes)<sup>28,34–38</sup>. Thus, flattening or clustering of *caveolae* enables PM reservoirs to accommodate changes in PM tension<sup>34</sup>. A component strictly required for caveolae formation in most cell types is caveolin-1 (Cav1)<sup>39</sup>, a hairpin-shaped, cholesterol-binding membrane protein that critically contributes to the scaffolding of the caveolar structure and contributes to lipid trafficking across different cell compartments<sup>40–44</sup>.

Mutations in caveolar components have a profound impact on adipose tissue physiology. Genetic disruption of Cav1 leads to a severe lipodystrophy syndrome in humans<sup>11,45–48</sup> and reduces fat mass in mouse models<sup>49</sup>. Atrophic Cav1<sup>-/-</sup> adipocytes show reduced size, increased sensitivity to lipotoxicity and cell death, and are surrounded by increased interstitial collagen deposits *in vivo*<sup>48,50</sup>, correlating with a limited expansion capacity of Cav1-null adipose tissue. Mutations in another essential caveolae component, Cavin-1 (polymerase I and transcript-release factor, PTRF) are also causative of lipodystrophy in humans<sup>51–59</sup>, suggesting that specifically the caveolar structure is relevant for adipocyte function and its disruption underlies these phenotypes. However, whether the mechanosensitive and mechanoprotective role of caveolae are important for adipose tissue expandability is not known.

First identified as a major Src-kinase target<sup>25,60,61</sup>, Cav1 Y14 residue is an important determinant in Cav1-dependent processes, such as Rho-driven integrin-mediated adhesion and cell migration<sup>62–64</sup>, or insulin/growth factor response<sup>65–69</sup>. Of note, phosphorylation on Cav1 Y14 residue has been involved in the cell response to osmotic and oxidative stress<sup>70</sup>, suggesting that cell volume regulation may be acting upstream of this residue; Y14 phosphorylation has been shown to be induced by mechanical stimuli and to play a role in different signaling pathways<sup>38,71–74</sup>. Recently, studies using exogenous constructs suggested that Y14 phosphorylation might control, in part through electrostatic forces, caveolar structure<sup>74</sup>. However, the role of this residue and its effects on caveolae biology *in vivo* remain unknown.

Here, we show that adipocyte PM ultrastructure adapts to lipid droplet (LD) expansion *in vivo*. As the lipid droplet grows, caveolae are deformed and disassemble, providing the additional membrane required to accommodate LD expansion. Caveolae absence generates rigid and less deformable adipocytes, which are prone to rupture upon mechanical constraint. Notably, Cav1 Y14F adipocytes show a diminished LD expansion-induced caveolae disassembly and accumulate deformed, pickle-shaped caveolae in regions of high PM-LD proximity. Y14F Cav1 mice show reduced visceral depots, smaller adipocytes and stiffer adipose tissue, evidencing the relevance of this residue for *in vivo* adipose tissue biology. Overall, our data suggest that adipocyte mechanoadaptation is mediated by caveolae *in vivo* and that PM physical characteristics contribute to the lipodystrophy phenotype in Cav1-depleted or mutated animal models.

## Results

### Expansion of the LD reorganizes adipocyte surface ultrastructure *in vivo*

Adipocytes accommodate large amounts of fat within LDs, resulting in a significant volume increase<sup>75</sup>. As a result, adipocyte PM is stretched and likely adapts by unknown mechanisms to withstand volumetric changes. We hypothesized that caveolae could be important for PM adaptation to the physical alterations derived from LD growth. To understand caveolae response during adipose tissue growth, and their possible role ensuring safe LD expansion, we analyzed adipocyte ultrastructure by electron microscopy (EM) and precisely quantified the organization of caveolar domains and their behavior as a function of LD growth across an extensive image collection (5018 EM images) capturing the cell surface of 133 cells (Supplementary Fig. 1a) as spatially related to other structures including the PM and the LD surface. We quantified different types of caveolar domains and classified them into three categories: single-pit caveolae (individual caveolae with a neck), rosettes (caveolae clustered within a common invagination) and cavicles (vesicles, where the connection with the PM or with a rosette was not evident) (Fig. 1a)<sup>36,37,76</sup>. All these structures were labeled with gold particles directed against Cav1 (Supplementary Fig. 1b) and were absent in Cav1-null cells (Supplementary Fig. 1c) suggesting they all were caveolar structures. Although many of these structures are apparently disconnected from the PM, they are known to be mostly connected with the cell surface, thus representing PM caveolar structures<sup>36,37,77,78</sup>.

Quantification of caveolar structures in mouse epididymal adipocytes revealed that caveolae density varied between 0.93 and 9.13 caveolae/ $\mu\text{m}$ , with a median caveolar density of 3.42 caveolae/ $\mu\text{m}$  (inter quartile range (IQR) 4.73–2.58). For the different caveolar categories, we obtained a median of 1.31 single pit/ $\mu\text{m}$  (IQR 1.70–0.94), 0.79 rosette/ $\mu\text{m}$  (IQR 1.35–0.36), and 1.16 cavicle/ $\mu\text{m}$  (IQR 1.78–0.80).

We noticed that caveolar structures were not randomly distributed in space. Rather, adipocytes whose LD is relatively far from the PM, accumulated more caveolar domains (Fig. 1b). To precisely quantify this observation, we analyzed in detail the distribution of caveolae with respect to PM-LD distance. First, we classified caveolar structures and determined PM-LD distance through every caveolar coordinate (Supplementary Fig. 1d). This analysis indicated that PM-LD distance through rosettes and cavicles was larger, as compared to single-pit caveolae (Fig. 1c). This was expected since rosettes and cavicles represent complex, multilobed caveolar clusters that penetrate deep into the cytosol<sup>28,36,37,77,78</sup>, while single-pits do not require much space and they can fit in regions of shorter PM-LD distance.

Next, we computed relative caveolae density for each adipocyte, and found a strong positive correlation between total caveolae counts per  $\mu\text{m}$  of cell perimeter, and median PM-LD distance (Fig. 1d). Similar correlations were found for rosettes and cavicles (Fig. 1e, f). Thus, adipocytes with short distance between the PM and the LD had reduced rosette and cavicle numbers, indicating that rosettes and cavicles disassembled in response to LD expansion, consistent with their localization in regions of higher PM-LD distance (Fig. 1c). We found no apparent response for single-pits, which remained constant independently of PM-LD distance (Fig. 1g). However, the frequency distribution of PM-LD distances shows extreme values that are concealed when obtaining the median for each cell (Supplementary Fig. 1e). To account for this, we analyzed the abundance of caveolar domains in different ranges of PM-LD distance, normalized by the frequency of those distance ranges in the sample (Fig. 1h). This analysis revealed that rosettes and cavicles start to disappear when PM-LD distance reaches around 1.5 microns, and their number steadily diminishes with further approximation of the LD. Interestingly, while single-pits remained largely unaffected through LD-PM approximation, they show a clear and abrupt disappearance when the distance decreased below 80 nm. Within this distance range, caveolae

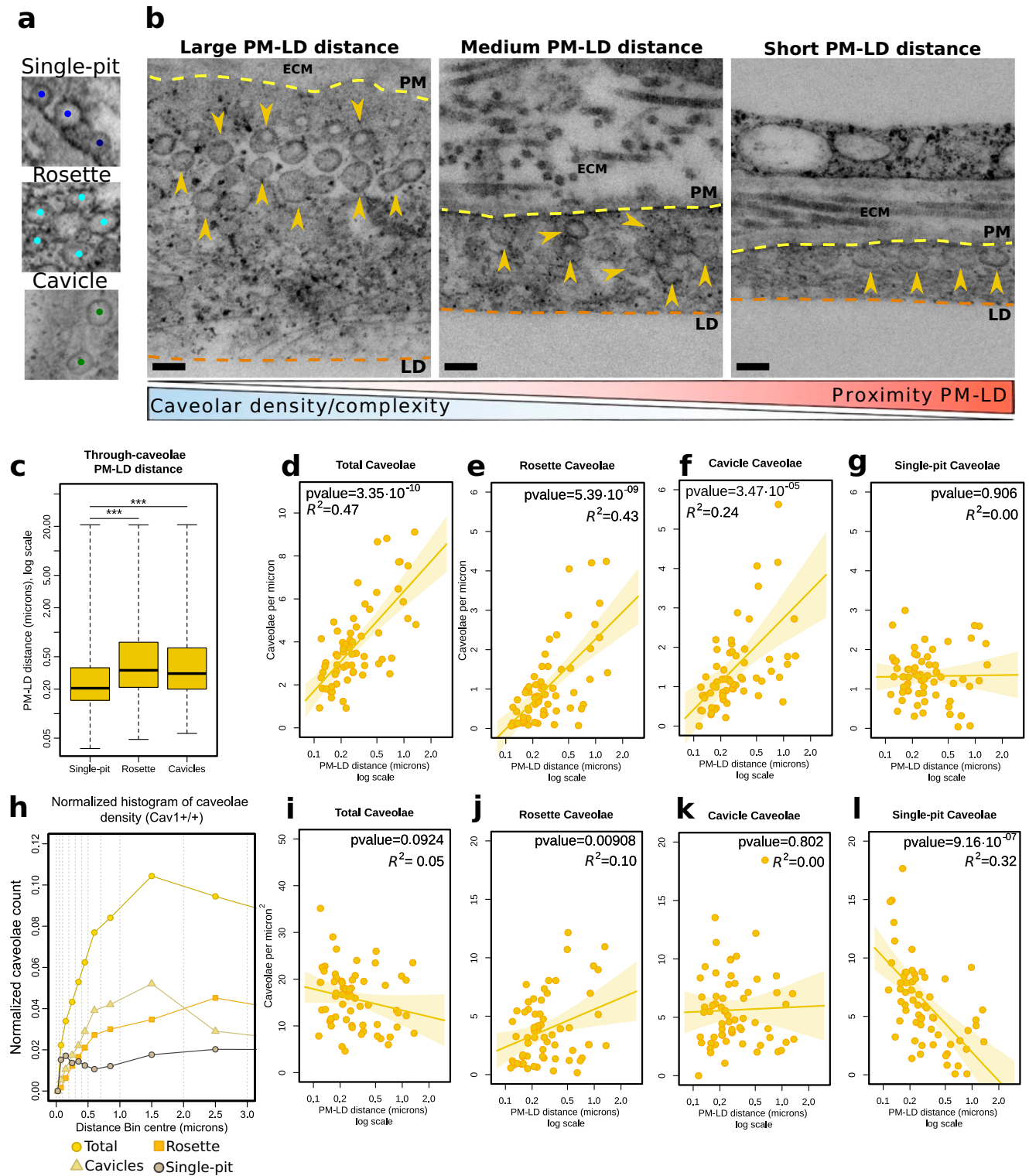


**Fig. 1 | Expansion of the LD reorganizes PM ultrastructure in vivo.** **a** Examples of caveolae identification and classification. **b** PM-LD impacts density and complexity of caveolar domains. Scale bar: 100 nm. **c** Distance at caveolar coordinates (as calculated in Supplementary Fig. 1c.2) for different caveolae types. Sample size: 6908 single-pit, 6362 caveolae in rosettes, 8729 cavicles. Individual datapoints and boxplot outliers were removed in the representation for simplicity. Boxplot boxes represent first, second (center), and third quantile. Box whiskers expand to the full range of data. The representation shows the distribution of all caveolae in the sample, but statistical analysis was performed comparing median through-caveolae distance by cell with paired Wilcoxon sign rank test (sample size: 64 cells,  $p$  values:  $3.9 \times 10^{-5}$  for rosette and single-pit comparison,  $1.7 \times 10^{-7}$  for cavicle and single pit comparison).

**d–g** Caveolae density measured as caveolae/ $\mu$ m of cell perimeter for total caveolae (**d**), caveolae in rosettes (**e**), cavicles (**f**) and single-pit caveolae (**g**). Sample size=64.  $p$  values shown for the null hypothesis slope=0. For **d–g** error bands show 95% confidence interval for the estimation of the mean (line). **h** Caveolae counts in regions of increasing PM-LD distance, normalized by the frequency of the regions in the sample. **i–l** Spatial concentration of caveolae measured as caveolae/ $\mu$ m<sup>2</sup> for total caveolae (**i**), rosette caveolae (**j**), cavicles (**k**), and single-pits (**l**) as a function of median PM-LD distance. Each dot is an individual cell. Sample size = 64 cells.  $p$  values shown for the null hypothesis slope=0. For **i–l** error bands show 95% confidence interval for the estimation of the mean (line).  $p$ -value codes: \* $<0.05$ , \*\* $<0.01$ , \*\*\* $<0.001$ . All tests are two-sided. Source data are provided as a SourceData.zip.

frequency was consistently lower than expected from the average caveolae density in the sample (Supplementary Table 1). Thus, single-pits are also sensitive to LD growth but only at distances below approximately 80 nm.

To further understand the dynamics of caveolae disassembly upon LD-PM approximation, we computed caveolae spatial concentration by normalizing caveolae counts per squared micron of cytosolic area (LD excluded, as in Supplementary Fig. 1d). In this type of representation, a negligible slope would mean caveolar disassembly at a rate similar to LD expansion; a negative slope would mean caveolae accumulation with LD-PM proximity, and a positive slope would mean a disassembly rate faster than LD approximation (Supplementary Fig. 1f). This analysis showed that total caveolae per  $\mu\text{m}^2$  remained largely unchanged with LD-PM approximation, meaning that caveolae disappeared at a rate similar to LD expansion rate, keeping caveolae concentration constant (Fig. 1i). However, rosette concentration per  $\mu\text{m}^2$  decreased significantly as median PM-LD distance became smaller, suggesting that they disassembled at a higher rate than LD approximation (Fig. 1j). Cavicle amount per  $\mu\text{m}^2$  remained constant, meaning that they disassembled at the same pace as the PM was approached by the LD (Fig. 1k) and single-pits accumulated, indicating that they are largely refractory to LD approximation despite the decrease in available cytoplasmic space (Fig. 1l), consistent with the analysis of caveolar density per PM perimeter (Fig. 1d–g). Taken together, these results suggest that rosettes and cavicles are the first caveolar structures that respond to LD approximation, while single-pits respond specifically when LD-PM distance reaches the average caveolar diameter<sup>79</sup>.

LD approximation to the PM severely reduces the space in the cytosol where caveolae are located, which could lead to a compression in these structures, facilitating their disassembly; if this were the case, we would expect morphological alterations in caveolae induced by LD proximity. Considering that the filling of the LD is a relatively slow process, contrary to sudden cell stretching in muscles<sup>28</sup>, increased blood flow in vessels<sup>30</sup> or hypo-osmotic cell swelling<sup>29,36</sup>, we expected a relatively slow caveolae disassembly process, allowing for the visualization of potential transition morphologies. Following this logic, we compared the overall caveolae morphology with the morphology of caveolae on regions of short PM-LD distance. As shown in Fig. 2a, in areas of short LD-PM distance (<100 nm), caveolae acquired a flattened, elongated, pickle-shaped morphology, less circular than standard caveolae (Fig. 2a). These pickle-like caveolae were invariably elongated across an axis parallel to the PM perimeter, and perpendicular to the direction of the LD expansion, as if the LD was pushing them against the PM (Fig. 2b). These atypical structures were positive for immunogold staining against Cav1 (Supplementary Fig. 2a) and were absent from *Cav1*<sup>-/-</sup> samples (Supplementary Fig. 2b), suggesting they were formed by Cav1. Interestingly, these invaginations were, in some instances, in apparent direct contact to the LD surface, with no cytoplasmic space separating LD from PM (Fig. 2a, b). Quantification of caveolae morphology indicated that, in areas of short PM-LD distance, caveolae presented a reduced circularity (Fig. 2c), reduced area (Fig. 2d), and reduced perimeter and minor axis (Fig. 2e, f), while the neck width was slightly increased (Fig. 2g). Collectively, these results suggest that LD approximation to the PM induces a reorganization of the cell surface, involving caveolae deformation and disassembly.

To obtain further evidence of LD-induced caveolae disassembly, we analyzed in vitro Cav1 redistribution upon LD growth using TIRF microscopy (TIRFM). This approach has been used to infer caveolae flattening upon osmotic swelling in cultured cells<sup>29</sup>. We cultured primary, in vitro differentiated adipocytes in lipid-rich media for increasing periods of time, which induced BODIPY accumulation and an increase in mean LD area, reflecting intracellular fat accumulation overtime (Supplementary Fig. 2c, d). This process led to a progressive reduction in the intensity of Cav1 spots in the TIRFM plane (Fig. 2h, i). Moreover, the intensity of Cav1-positive spots observed by TIRFM was

clearly reduced in the center of the LD, a region with the shortest PM-LD distance assuming a spherical LD morphology (Fig. 2j, k). The effect was specific for the pool in the TIRFM plane, as Cav1 epifluorescence intensity (which captured all Cav1 pools) did not follow a clear trend (Supplementary Fig. 2e). Thus, the expanding LD induces a reduction in the intensity of Cav1 vesicles in the TIRFM plane, analogous to changes associated with hypoosmotic shock in in vitro differentiated adipocytes (Supplementary Fig. 2f), as well as other cell lines as reported<sup>29</sup>.

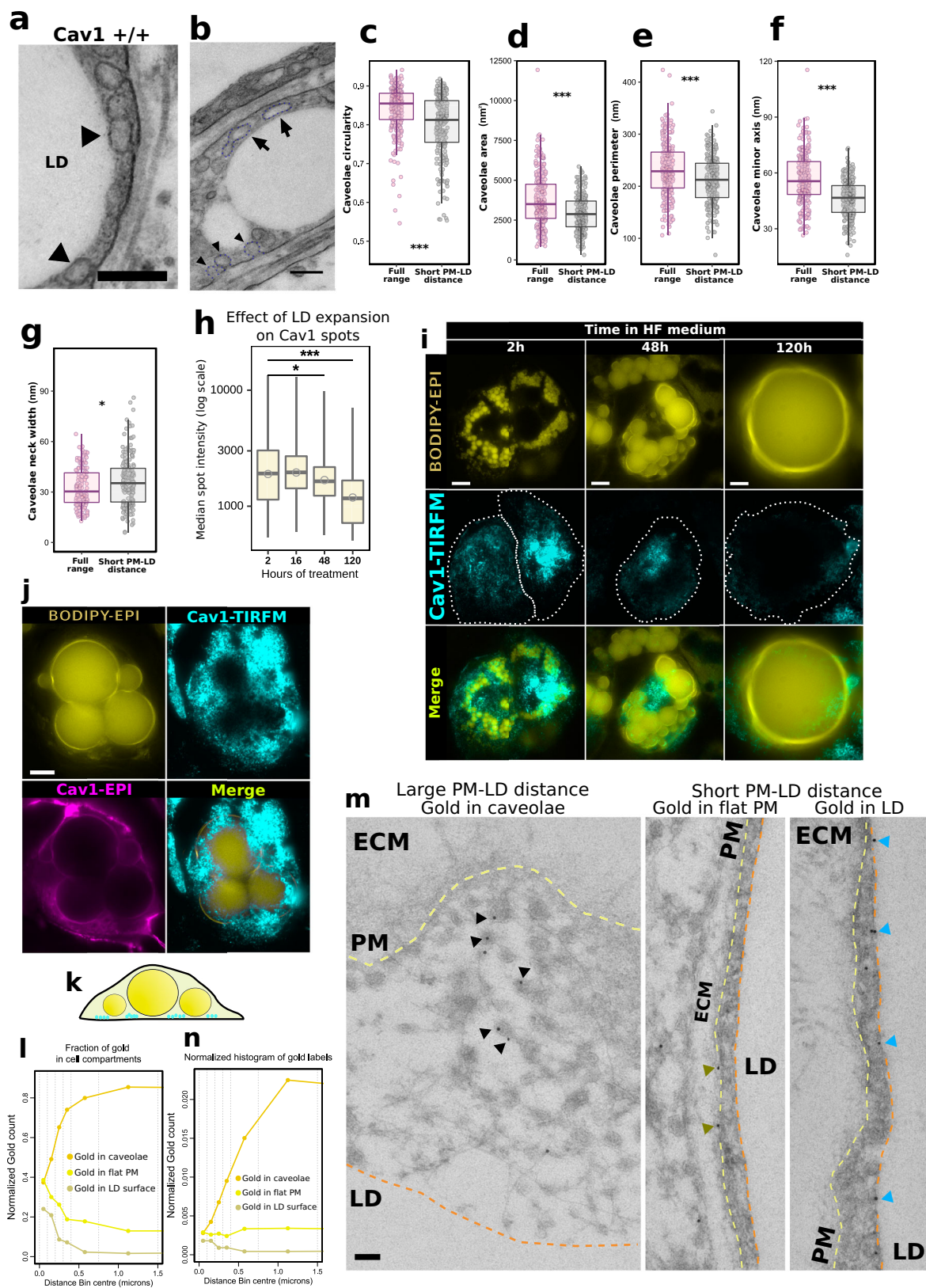
To understand where Cav1 was relocating to upon caveolae disassembly, we stained adipose tissue with anti-Cav1 immunogold and analyzed its location by EM. We then obtained normalized histograms for gold particle counts, and correlated gold counts with median PM-LD distance, analogous to what we previously did for caveolae. We found that the fraction of gold particles in caveolae decreased with PM-LD proximity, while the fraction of gold labels in flat PM and LD surface increased (Fig. 2l, m). In fact, in adipocyte regions where the LD is far from the PM, a high percentage of Cav1 (>80%) is apparently located in caveolae, while in regions where the LD is close to the PM the fraction of Cav1 in caveolae falls below 40% and the fraction of Cav1 located in the LD and flat PM reaches >60% (Fig. 2l). This process was driven by a clear decrease in gold particles associated with caveolae in absolute numbers (Fig. 2n, Supplementary Fig. 2g), consistent with the ordinary analysis of caveolar structures by EM (compare Figs. 2n to 1h). Gold labels in the LD surface underwent an increase with PM-LD proximity also in absolute numbers (Fig. 2n and Supplementary Fig. 2h), while gold labels at flat PM showed no clear tendency in absolute numbers (Fig. 2n and Supplementary Fig. 2i). Thereby, concomitant to the disassembling of caveolar domains there was a relocation of Cav1 to the LD surface and an increase in the fraction of golds located at flat PM regions (Fig. 2m, l). Collectively, these results suggest that caveolar domains, particularly rosettes and cavicles, are highly sensitive to LD proximity and flatten by the action of LD approximation. As a result, PM-LD distance inversely correlates with caveolar density and complexity (Fig. 1b).

### Cav1 regulates the mechanical properties of the adipose tissue

To understand how the severe PM remodeling observed during adipocyte expansion affects adipose tissue properties and adipocyte mechanoadaptation, we used a caveolae null (*Cav1*<sup>-/-</sup>) mouse model, which shows reduced adiposity and small adipocytes (Fig. 3a) as previously reported<sup>49</sup>. Interestingly, *Cav1*<sup>-/-</sup> adipocytes assessed by TEM showed increased average PM-LD distance, as compared to *Cav1*<sup>+/+</sup> controls, suggesting that, apart from being smaller, these adipocytes do not reach the same loading capacity as *Cav1*<sup>+/+</sup> adipocytes (Fig. 3b).

Based on our in vivo analysis of adipocyte PM ultrastructure, LD-PM approximation occurs concomitant with a disassembly of around 90% of caveolae (Fig. 1d). We estimated that the release of membrane contained in these caveolar structures would lead to a 3.95-fold increase in cell volume (see methods for details on the calculations). This membrane release could assist adipocyte volume oscillations during LD growth and contribute to its mechanoadaptation, thus explaining adipocyte size reduction in the absence of caveolae.

Cav1 absence could impair adipocyte hypertrophy by other means. Previous studies reported altered lipid uptake for Cav1-depleted fibroblasts<sup>80</sup> and EHD2 knockout mice<sup>81</sup>, which could account for the reduced hypertrophy observed in *Cav1*<sup>-/-</sup> adipocytes. Our EM data also suggest that *Cav1*<sup>-/-</sup> adipocytes could present a lower loading state (Fig. 3b). However, we did not observe any defect in lipid uptake in *Cav1*<sup>-/-</sup> adipose tissue explants during a short overnight exposure to the labeled fatty palmitate BODIPY 555/568 C<sub>12</sub>, which was incorporated by *Cav1*<sup>-/-</sup> adipocytes at equal or even increased rates as compared to wild type cells (Supplementary Fig. 2j, k). Thus, absence of Cav1 does not impair steady-state fatty acid intake in adipocytes, and other mechanisms must prevent sustained LD expansion.



Another potential explanation for reduced expandability in *Cav1*<sup>-/-</sup> adipocytes is the increased collagen deposition observed in *Cav1*<sup>-/-</sup> adipose tissue<sup>49,50</sup>: interstitial fibrosis poses a potential mechanical constraint for adipocyte hypertrophy<sup>15,82,83</sup>. To determine whether collagen deposition was a relevant factor limiting adipocyte growth in the absence of caveolae, we performed Masson's Trichrome staining of

sections from fat depots from wild type and *Cav1*<sup>-/-</sup> mice, and then classified adipocytes according to the presence or absence of collagen (blue staining) in their surroundings. Adipocytes were classified as fibrotic (FIB) when they were in contact with collagen (Fig. 3c asterisks), and non-fibrotic (NOFIB) when they were not (marked with an arrowhead). As expected, this method confirmed an increase of

**Fig. 2 | LD expansion reorganizes caveolar domains and morphology in vivo.** **a** Examples of low-circularity caveolae. **b** Elongated caveolae in PM-LD proximity (arrows) and circular caveolae for comparison (arrowheads). Caveolae perimeter is highlighted by a dotted line. Scale bar for **a** and **b**: 200 nm. **c–g** Caveolae morphological parameters: circularity (**c**), area (**d**), perimeter (**e**), minor axis (**f**), and neck (**g**). Sample size for full range and proximity regions, respectively: 259 and 233 caveolae for **c–f**, 152 and 174 for **g** (some caveolae did not have visible necks). For **c–g** wilcoxon test *p* values:  $3.7 \times 10^{-11}$ ,  $5.0 \times 10^{-8}$ ,  $9.7 \times 10^{-5}$ ,  $2.2 \times 10^{-16}$ ; 0.04. **h** Median intensity of TIRFM Cav1 spots in in vitro differentiated adipocytes during increasing times of lipid loading. Sample size from 2 to 120 h: 369, 365, 268, 247 cells. Experiment performed twice. Dunn's test with Bonferroni correction *p* values for comparison with 2-hour timepoint from left to right: 1, 0.04,  $1.1 \times 10^{-21}$ . **i** Representative examples of in vitro differentiated adipocytes in increasing times of lipid loading. **j** in vitro differentiated adipocytes after 120 h of HF treatment

showing decreased intensity of Cav1 spots in LD centers. Scale bar for **i, j**: 10  $\mu$ m. **k** Schematical representation of theoretical LD lateral view, showing shorter PM-LD distance at LD center. **l** Gold label counts in caveolae, flat PM and LD surface in regions of increasing PM-LD distance, normalized by the total cellular gold label counts in the same region. **m** Examples of preferential location of gold labels in caveolae (black arrowheads) in regions of large PM-LD distance, and preferential location of gold labels in flat PM (brown arrowheads) and LD surface (blue arrowheads) in regions of short PM-LD distance. Scale bar: 100 nm. **n** Gold label counts in regions of increasing PM-LD distance, normalized by the frequency of the regions in the sample. *p*-value codes: \* <0.05, \*\*<0.01, \*\*\*<0.001. All boxplots show first (Q1), second (median), and third (Q3) quantiles, and whiskers extend from Q1-1.5-IQR (interquartile range) to Q3+1.5-IQR except for **h**, where they expand to the full range of data. Circles indicate average. All tests are two-sided. Source data are provided as a SourceData.zip.

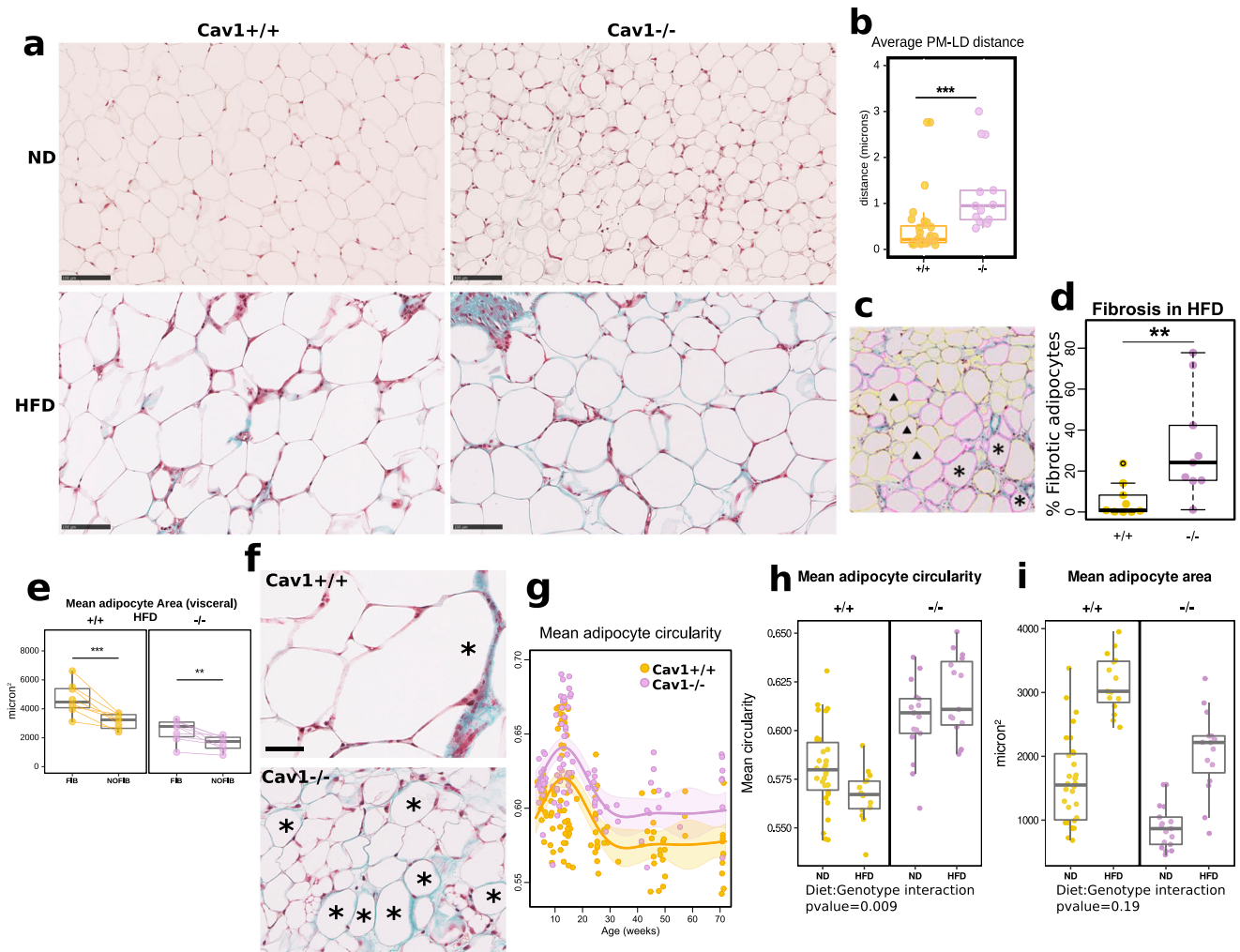


**Fig. 3 | Cav1 regulates adipocyte morphology and deformability.** **a** Masson's Trichrome staining of epididymal VAT. Scale bar: 100  $\mu$ m. **b** Average adipocyte PM-LD distance in EM images. *N* = 31+/+, 13/- adipocytes, wilcoxon test *p* value =  $3.6 \times 10^{-5}$ . **c** Adipocyte classification based on the existence (magenta, asterisks) or absence (yellow, triangles) of surrounding collagen. **d** Percentage of fibrotic epididymal VAT adipocytes of 45 weeks-old HFD animals. Wilcoxon test *p* value = 0.002, *n* = 9 animals. **e** Influence of surrounding fibrosis in adipocyte area. Lines join average adipocyte values for depots from the same animal. Paired *t*-test *p* values: 0.0007 for +/+ (8 animals) and 0.0012 for -/- (9 animals). **f** Examples of fibrotic (asterisks) and non-fibrotic adipocytes. Scale bar: 50  $\mu$ m. **g** Adipocyte mean

circularity during aging, with 95% confidence intervals. Sample size: 123+/+, 98-/- animals. Effect of diet on adipocyte circularity (**h**) and area (**i**) in 45-week-old animals. *t*-test for regression coefficients *p*-values: effect of diet in WT circularity and area, 0.028 and  $6.50 \times 10^{-14}$ , respectively; diet-genotype interaction, 0.009 for circularity and 0.19 for area. Sample size for **h** and **i**: For ND, 30 animals +/+ and 17 -/-; for HFD, 15 per genotype. Boxplots show first (Q1), second (median), and third (Q3) quantiles, and whiskers extend from Q1-1.5-IQR to Q3+1.5-IQR. *p*-value codes: \* <0.05, \*\*<0.01, \*\*\*<0.001. All tests are two-sided. Source data provided as a SourceData.zip.

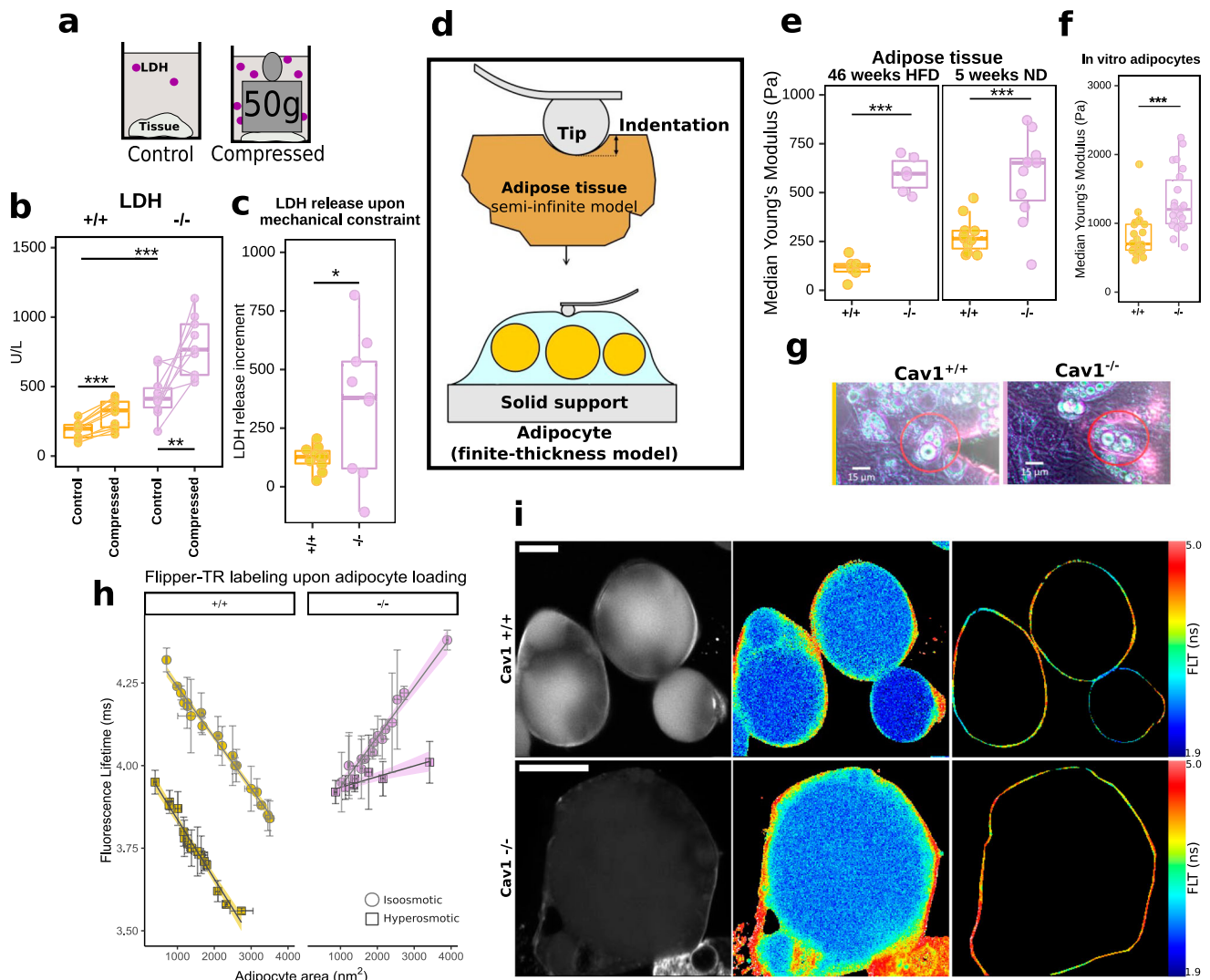


**Fig. 4 | Cav1 regulates adipocyte mechanical properties.** **a** Schematic representation of compression assay on VAT. **b** LDH activity in media. Lines connect control and compressed contralateral depots of the same animal, paired *t*-test *p* values:  $4.2 \times 10^{-5}$ , 0.0071 (comparison between contralateral depots). Pairwise *t*-test with Bonferroni correction *p* value: 0.00017 (comparison between genotypes). **c** LDH activity difference between stimulated and control contralateral depots. Pairwise *t*-test with Bonferroni correction *p* value = 0.039. Sample size for **k** and **l**: 10<sup>+/+</sup> and 9<sup>-/-</sup> animals, **d** Schematic cross-sections of AFM-based force spectroscopy (indentation) experiments with bottom-effect corrections<sup>143</sup>. Median Young's Modulus for VAT (**e**) and in vitro differentiated adipocytes (**f**). For **n** and **o**: pairwise

*t*-test *p* values:  $2.2 \times 10^{-7}$  for HFD (6 animals), 0.00035 for ND (11 animals), 0.00033 for cells (22 cells from 4 animals per genotype). **g** Examples of adipocytes selected for AFM. **h** Flipper-TR FLT as a function of adipocyte area. Sample size for isoosmotic: 24<sup>+/+</sup>, 21<sup>-/-</sup> hyperosmotic: 17<sup>+/+</sup>, 14<sup>-/-</sup> cells. Average FLT and area for different *z* of the same cell  $\pm$ SEM is represented. **i** Examples of Flipper-TR FLT after 120 h of HF media treatment and manually segmented membranes. Scale bar: 20 microns. Boxplots show first (Q1), second (median), and third (Q3) quantiles, and whiskers extend from Q1-1.5-IQR to Q3+1.5-IQR. *p*-value codes: \* $<0.05$ , \*\* $<0.01$ , \*\*\* $<0.001$ . All tests are two-sided. Source data provided as a SourceData.zip.

fibrotic adipocytes in *Cav1*<sup>-/-</sup> tissues (Fig. 3d). We next computed adipocyte area and analyzed its correlation with either presence or absence of collagen in its surroundings. Surprisingly, the area of fibrotic adipocytes was bigger as compared to non-fibrotic ones, and this was observed in both genotypes (Fig. 3e, f). Therefore, the increased fibrosis observed in *Cav1*<sup>-/-</sup> tissues could not account for the reduced adipocyte area of *Cav1*<sup>-/-</sup> adipocytes (Fig. 3a). Thus, the results presented here support that caveolae absence impairs adipocyte hypertrophy by mechanisms independent of lipid uptake and collagen deposition.

Of note, concomitant with impaired hypertrophy, absence of Cav1 also led to alterations in cell morphology, since caveolae-depleted adipocytes were more circular independently of age (Fig. 3a, g). Control adipocytes underwent a decrease in circularity upon High Fat Diet (HFD) treatment (Fig. 3h, *p*-value = 0.028, Supplementary Table 2),

together with an expected area increase, indicating that adipocyte shape is altered during expansion (Fig. 3h, i). Interestingly, cells lacking caveolae underwent a comparable increase in area in HFD (Fig. 3i, *p*-value for Genotype:Diet interaction = 0.19 Supplementary Table 2), but remained highly circular (Fig. 3h, *p*-value for Genotype:Diet interaction = 0.00865 Supplementary Table 2), suggesting that Cav1 regulates adipocyte deformability upon LD expansion. Of note, circularity reduction favors efficient adipocyte spatial stacking (Supplementary Fig. 2l). A simple theoretical calculation demonstrates that perfectly circular adipocytes would only cover up to 90.7% of tissue area (Supplementary Fig. 2l, m, see "Materials and methods" section for details) while more polygonal shapes could cover a higher space percentage (Supplementary Fig. 2m, Fig. 3a). Thus, caveolae assist adipocyte shape flexibility during expansion, facilitating optimal cellular stacking within the tissue.

*Cav1*<sup>-/-</sup> adipocytes are known to be more fragile at basal conditions<sup>50</sup> but their resistance and adaptability to mechanical stress is not known. Fat tissue is exposed to compression forces and plays a role in mechanoprotection of other organs<sup>84</sup>. We performed compression assays on epididymal fat depots and measured lactate dehydrogenase (LDH) release, a widely used marker of tissue damage (Fig. 4a)<sup>18,50,85–90</sup>. *Cav1*<sup>-/-</sup> adipose tissue explants exhibited higher LDH release values in basal conditions as compared to *Cav1*<sup>+/+</sup> controls, consistent with previous reports (Fig. 4b)<sup>50</sup>. Mechanical compression in both genotypes increased LDH release, suggesting cell rupture (Fig. 4b). LDH increase after compression was significantly higher in *Cav1*<sup>-/-</sup> tissues (Fig. 4c), suggesting that lack of caveolae renders adipose tissue more susceptible to cell rupture upon mechanical challenge.

The altered deformability and increased fragility observed in *Cav1*<sup>-/-</sup> adipocytes hint to a defect in mechanical adaptability. To test this possibility, we extracted epididymal visceral adipose depots from old animals (45–46 weeks) fed with high fat diet (HFD) and analyzed them by AFM-based nanoindentation experiments<sup>91</sup> (Fig. 4d). We observed a three-fold increase in the Young's modulus of tissues lacking Cav1 as compared to those from wild type animals. In other words, the absence of Cav1 was associated with an increase in tissue rigidity (Fig. 4e). These measurements were replicated in tissues from young, 5 weeks-old animals fed with normal diet, obtaining again that the elastic modulus was higher for *Cav1*<sup>-/-</sup> tissues, implying that the mechanical alterations appeared early in adipose tissue development and were independent on the age or dietary treatment (Fig. 4e). To rule out whether the enhanced fibrosis observed in the *Cav1*<sup>-/-</sup> tissue was contributing to increased elastic modulus, we performed AFM-based nanoindentation measurements also on adipocytes differentiated in vitro (Fig. 4f, g). This allows to minimize the potential effects from the adipocyte micro-environment, extrinsic to adipocyte mechanical properties. In vitro-differentiated *Cav1*<sup>-/-</sup> adipocytes were also significantly stiffer (Fig. 4f), suggesting that these mechanical phenotypes are cell-intrinsic and independent from the development of fibrosis.

The AFM technique, however, does not allow us to discriminate between the contributions of the different cellular components to cell stiffness. In order to describe the biomechanical properties of the adipocyte cell membrane, we used the cell membrane tension probe Flipper-TR<sup>92</sup>. Longer fluorescence lifetime (FLT) of the probe correlates with increased stiffness. When applied to adipocytes loaded with high-fat media, Flipper-TR FLT at the cell membrane decreases with adipocyte cell area in *Cav1*<sup>+/+</sup> adipocytes, while showing the opposite tendency in *Cav1*<sup>-/-</sup> (Fig. 4h). As a result, absence of Cav1 in big, unilocular adipocytes leads to increased FLT in the adipocyte membrane, indicating increased stiffness as compared to controls (Fig. 4h, i). To further confirm that Flipper FLT is indicative of membrane tension in our cell type, we performed the same experiment upon addition of hyperosmotic media (Fig. 4h), which is expected to decrease membrane tension; as expected, FLT decreased in this setting (Fig. 4h and Supplementary Fig. 2n, o). It must be noted however that the Flipper-TR probe is also sensitive to the biochemical environment, meaning that FLT is affected by PM lipid composition and varies across cell types<sup>92</sup>. Cav1 affects cholesterol distribution and lipid organization at the PM<sup>93</sup>. This is a parameter that, at present, we cannot dissect from purely mechanical effects when directly comparing Cav1 genotypes. Nonetheless, the opposite FLT slope and cell size correlation when comparing wild type to *Cav1*<sup>-/-</sup> adipocytes likely reflects the effect of caveolae buffering of membrane tension during adipocyte expansion: caveolae disassembly would facilitate a decrease in membrane tension during loading while, in absence of caveolae, membrane tension would build up as the adipocyte gets bigger. Collectively, these results support that Cav1 contributes to the mechanoadaptation of adipocytes, preserving adipocyte compliance, deformability and integrity.

## Cav1 Y14 modulates LD growth-induced caveolae disassembly

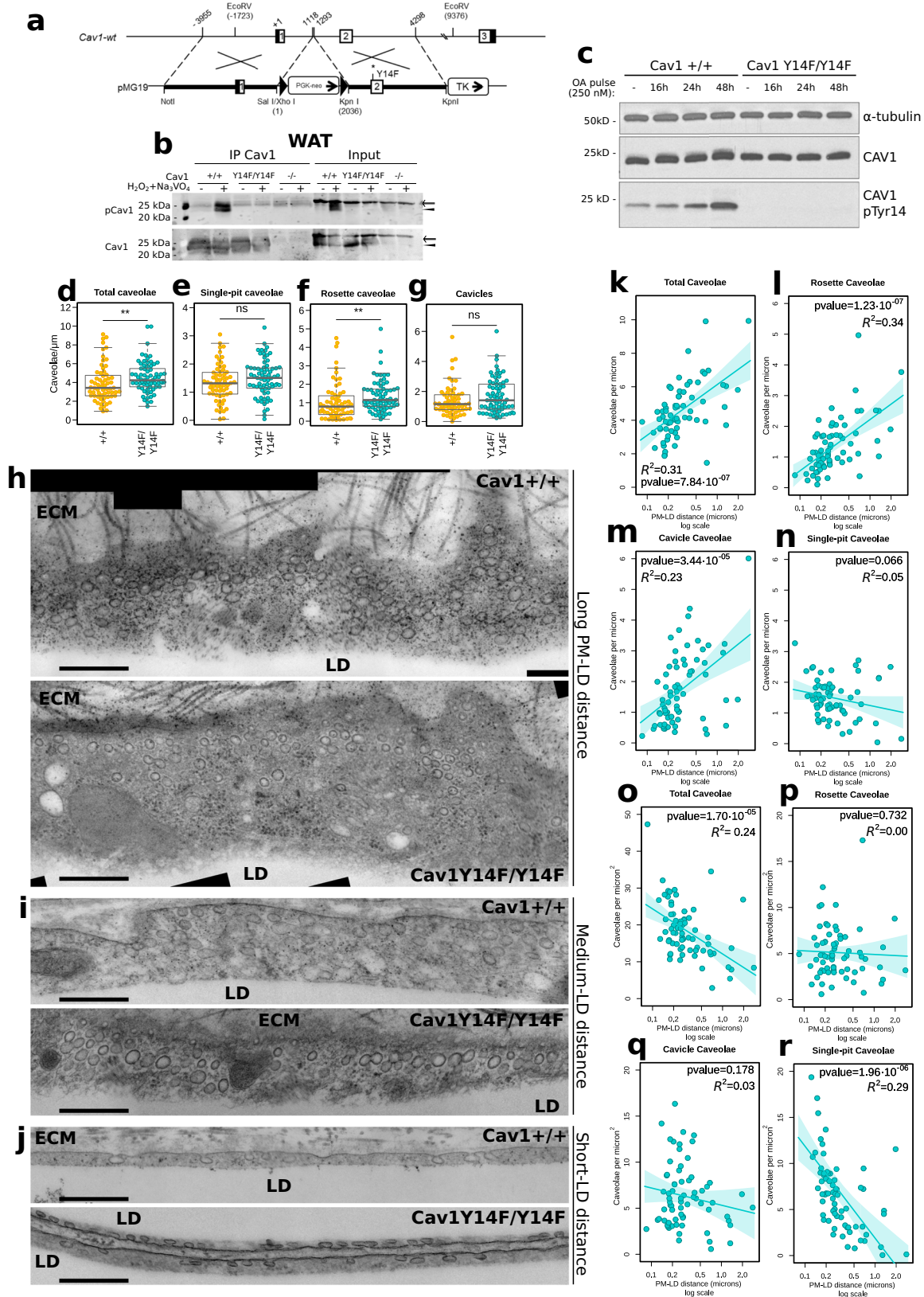
In order to deepen on the molecular mechanisms behind caveolae mechanoadaptation to LD growth, we focused on Cav1 and its phosphoregulated residue Y14. This residue plays an important role in several Cav1 functions as previously shown in vitro (reviewed in<sup>94</sup>), yet its role in vivo remains unknown. We generated a *Cav1*<sup>Y14F/Y14F</sup> mouse model following the strategy depicted in Fig. 5a (see “Materials and methods” section for details). As expected, Cav1 Y14F protein was non-phosphorylatable at its Y14 position, but nonetheless showed normal expression levels in WAT and primary mouse embryo fibroblasts (MEFs) (Fig. 5b and Supplementary Fig. 3a, b). Its subcellular distribution was similar to the wild-type protein in adipocytes (Supplementary Fig. 3c, d), WAT, pancreas and liver (Supplementary Fig. 3d). Importantly, we assessed relative Y14 phosphorylation levels upon oleate loading in in vitro differentiated 3T3-L1 (ATCC CL-173) adipocytes, genome-edited to exclusively express either wild type Cav1 or Y14F Cav1 mutant. A specific signal of enhanced Cav1 Y14 phosphorylation, correlating with loading time, was observable (Fig. 5c and Supplementary Fig. 3e).

As reported for other cell models, EM analysis indicated that *Cav1*<sup>Y14F/Y14F</sup> adipocytes formed caveolae (Supplementary Fig. 3f). Surprisingly, *Cav1*<sup>Y14F/Y14F</sup> adipocytes had higher caveolae density, as compared to the *Cav1*<sup>+/+</sup> controls (Fig. 5d). These differences were observed across all caveolar structure types, although only rosettes reached statistical significance (Fig. 5e–g). Since Cav1 and Cav1 Y14F protein levels were comparable (Fig. 5b), other factors controlling assembly/disassembly rate might explain these changes. Interestingly, there was no apparent difference in caveolae density at regions of long PM-LD distance (Fig. 5h), but *Cav1*<sup>Y14F/Y14F</sup> adipocytes showed higher caveolae numbers at regions of medium (Fig. 5i) and short (Fig. 5j) PM-LD distance, hinting to a diminished caveolar response to LD proximity. *Cav1*<sup>Y14F/Y14F</sup> caveolae disassembled as the LD approximated the PM (Fig. 5k); however, the disassembly rate was lower as compared to controls (control slope=2.0; Y14F slope=2.0–0.7; interaction *p*-value = 0.0546, Supplementary Table 3), confirming a delayed response. Similar to wild-type cells, *Cav1*<sup>Y14F/Y14F</sup> caveolae disassembly was mostly driven by rosettes and cavicles, while single-pits showed no overall response (Fig. 5l–n).

When caveolae were normalized per  $\mu\text{m}^2$  of cytoplasm (LD excluded), Y14F caveolae density increased with LD-PM approximation, suggesting a moderate resistance to LD-induced disassembling as compared to controls (Figs. 5o, 1i, Supplementary Table 4, control slope = -2.0; control slope *p*-value = 0.1; Y14F slope = -2.0–3.3; interaction *p*-value = 0.0434). As mentioned previously, *Cav1*<sup>+/+</sup> rosette density per  $\mu\text{m}^2$  positively correlated with PM-LD distance, meaning that they disassembled faster than LD approximation (Fig. 1j); on the contrary, for Cav1 Y14F rosettes the slope was negligible, indicating a delayed response (Fig. 5p, Supplementary Table 4, control slope=1.4; control slope *p*-value = 0.009; Y14F slope=1.4–1.6; interaction *p*-value = 0.03079). Overall cavicle and single-pit behavior was comparable for both genotypes (Figs. 5q, r, 1k, l). Analysis of caveolar categories across different distance ranges indicated that the relative accumulation of caveolae in *Cav1*<sup>Y14F/Y14F</sup> adipocytes as compared to wild-type cells was more evident, and statistically significant, at short PM-LD distances (below 300 nm of PM-LD distance, Fig. 6a). Rosette and cavicle contribution to this difference was evident below 200 nm of PM-LD distance (Fig. 6b, c), while single pits accumulated more in the region of 0–100 nm (Fig. 6d), which is the region where wild type single pits were sensitive to LD-PM proximity (see Fig. 1h, Supplementary Table 1). Collectively, these results suggest that Y14F caveolae show a diminished response to PM-LD proximity, and thus an increased accumulation, at regions of short PM-LD distance.

To confirm the effect of Y14 residue on caveolae disassembly in vitro, we imaged in vitro differentiated adipocytes by TIRF upon different times of high fat loading. To account for the possibility that





detected Cav1 spots could belong to extracaveolar Cav1 deposits, we quantified the percentage of Cav1 positive spots that colocalized with Cavin 1 positive spots, obtaining a clear decrease in colocalized spots over time, and particularly after 120 h of high-fat loading (Fig. 6e). The overall percentage of colocalized spots was higher in *Cav1*<sup>Y14F/Y14F</sup>, consistent with the increased caveolar density observed by TEM, and

its reduction with time was diminished (Fig. 6e, f). This supports a model whereby, as the adipocyte fills with fat, Cav1 and Cavin1 localization decreases, hinting to caveolae disassembly, and that this process is favored by Y14 residue.

Interestingly, caveolae circularity reduction at short LD-PM distance regions (<100 nm) was significantly stronger in *Cav1*<sup>Y14F/Y14F</sup>

**Fig. 5 | Cav1 Y14 is needed for LD expansion-induced caveolae reorganization.** **a** Targeting strategy for producing the Y14F conditional allele. The loxP sites are marked with triangles. TK: thymidine kinase gene for negative selection of ES clones by resistance to G418/ganciclovir. PGK-neo: neomycine resistance gene under the control of the phosphoglycerate kinase promoter. **b** Western blot analysis of Cav1 levels and phosphorylation in visceral WAT. Adipose tissue was treated with  $H_2O_2+Na_3VO_4$  to induce Y14 phosphorylation and contralateral depots used as controls, demonstrating lack of phosphorylation in Y14F animals. An unspecific band of 25 kDa was present in all WAT samples (arrow), and thus samples were additionally subjected to immunoprecipitation with an antiCav1 antibody. Arrowhead marks specific Cav1 band height. **c** Representative WB of total and pCav1 in +/- and Y14F/Y14F in whole lysates from in vitro differentiated 3T3-L1 adipocytes, genome-edited to exclusively express either wild type Cav1 or Y14F Cav1 mutant. **d–g** caveolae counts per  $\mu m$  of cell perimeter for total caveolae (**d**), single-pit

caveolae (**e**), caveolae in rosettes (**f**) and cavicles (**g**). **d–g** Wilcoxon signed rank test  $p$  values from left to right: 0.004, 0.123, 0.002, 0.138. Sample size=64/+ and 69 Y14F/Y14F cells. **h–j** Representative images of adipocyte caveolae at long (**h**), medium (**i**), and short (**j**) PM-LD distances. Scale bar: 0.5  $\mu m$ . **k–n** Caveolae density measured as caveolae/ $\mu m$  of cell perimeter for total caveolae (**k**), rosette caveolae (**l**), cavicle (**m**), and single-pits (**n**). Sample size=69 cells.  $p$  values shown for the null hypothesis slope=0. **o–r** Spatial concentration of caveolae measured as caveolae/ $\mu m^2$  for total caveolae (**o**), rosette caveolae (**p**), cavicles (**q**), and single-pits (**r**) as a function of median PM-LD distance. Each dot is an individual cell. Sample size=69 cells.  $p$  values shown for the null hypothesis slope=0. For **k–r** error bars show 95% confidence interval for the estimation of the mean (line).  $p$ -value codes: \* <0.05, \*\*<0.01, \*\*\*<0.001. All boxplots show first (Q1), second (median) and third (Q3) quantiles, and whiskers extend from Q1-1.5\*IQR to Q3+1.5\*IQR. All tests are two-sided. Source data provided as a SourceData.zip.

caveolae, as a result of an increased density of pickle-like caveolae (Figs. 6g and 5j and Supplementary Table 5). A possible interpretation for this is that delayed caveolae disassembly upon LD approximation leads to the accumulation of compressed, non-circular caveolae, which would represent an intermediate state towards flattening (Fig. 6h, i).

Immuno-gold EM analysis in *Cav1*<sup>Y14F/Y14F</sup> adipocytes indicated that the caveolar compartment retained a high fraction of gold labels throughout all PM-LD distance ranges, and the fraction of gold located at flat PM or the LD surface increased very slightly with PM-LD proximity, contrary to what we previously observed for the controls (Figs. 6j and 2l). In fact, Y14F/Y14F caveolae seem to retain near 80% of Cav1 in adipocyte regions across all PM-LD distances, while the fraction of Cav1 contained in PM and LD only surpass 20% in very short PM-LD distances (Fig. 6j). In absolute numbers, gold labels associated with caveolar structures decreased with PM-LD proximity (Fig. 6k), although to a lesser extent than in controls (Fig. 2n). Gold labels associated with flat PM and LD surface showed no clear tendency in absolute numbers with LD-PM approximation (Fig. 6k).

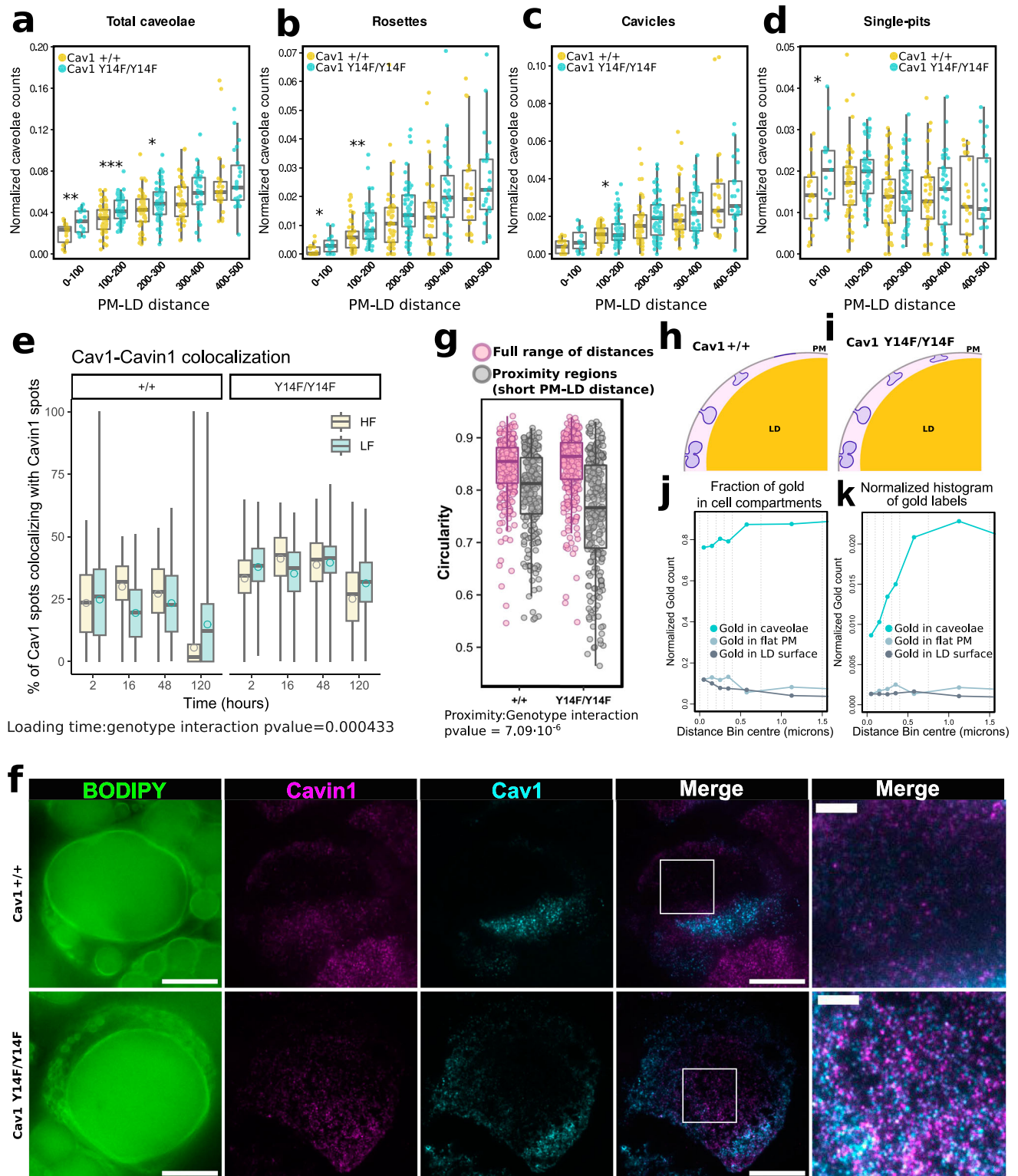
This hinted to a potential relocation of caveolar Cav1 to the LD surface upon LD approximation to PM. We purified LD-rich fractions by flotation through sucrose gradients as previously described<sup>95</sup> from 3T3-L1 (ATCC CL-173) cells genetically edited and rescued to either express wild-type Cav1 or Y14F Cav1 and differentiated in vitro (see above Supplementary Fig. 3e and Fig. 7a, b). As supported by previous studies describing the core LD proteome<sup>96</sup>, a fraction of Cav1 was consistently detected on purified LDs (Fig. 7a–c). Importantly, Cav1 relative levels on purified LDs increased upon oleate loading in wild type cells, but not in Cav1 Y14F-expressing cells (Fig. 7a–c). Of note, and in agreement with previous studies<sup>97</sup>, EHD2, but not Cavin-1, followed a similar behavior of Y14-dependent relative accumulation at LD-rich fractions (Fig. 7a–c). We observed analogous patterns when analyzing adipocyte cultures derived from in vitro differentiated primary precursors (Supplementary Fig. 3g). Consistent with these observations and in agreement with previous reports, exposure to Src inhibitor PP2 blunted Cav1 and EHD2 accumulation at LDs (Supplementary Fig. 3h). Moreover, Cav1 relocation to the LD in *Cav1*<sup>+/+</sup> cells occurred even in presence of the dynamin inhibitor Dyngo-4<sup>®</sup> (Supplementary Fig. 3i), suggesting that this process is independent of mechanisms regulating endocytosis (see Discussion).

In order to determine whether the rate of caveolae biogenesis could play a role in the observed caveolae disassembly upon LD expansion and the Y14F/Y14F phenotype, we subcloned GFP conjugated wild type or Y14F Cav1 in a doxycycline inducible vector in *Cav1*<sup>-/-</sup> fibroblasts, induced adipogenic differentiation during 8 days and acquired TIRFM images after 5 min of doxycycline protein induction. As a result, we found that the number of newly formed Cav1 vesicles was increased for the Y14F protein as compared to control (Fig. 7d–f), suggesting an increased caveolae assembly rate that could explain the increased caveolae numbers found by EM (Fig. 5d) and the increased number of Cav1 spots found by TIRF in *Cav1*<sup>Y14F/Y14F</sup>

adipocytes (Fig. 6e). Of note, the number of wild type Cav1 positive vesicles formed after 5 min of doxycycline induction were not significantly changed in fibroblasts treated with a pulse of oleate for 24 h prior to the experiment, indicating that lipid loading is unlikely to induce an impairment of caveolae biogenesis that could explain the reduced caveolae numbers observed after HF treatment in adipocytes (Figs. 7e, f, 2h, i, and 6e). Interestingly, the density of Cav1 positive vesicles was increased in regions overlapping with the LD, ruling out the possibility that the previously observed decrease in cav1 spots in LD proximity (Fig. 2i,j) can be attributed to a defect in caveolae biogenesis (Supplementary Fig. 3j). These results are also in agreement with previous reports showing increased caveolae formation upon high PM tension<sup>98</sup>. This effect of LD proximity on caveolae biogenesis was equivalent for both Cav1 WT and Cav1 Y14F clusters. These data suggest that Cav1 phosphoacceptor Y14 is involved in caveolae assembly dynamics.

To deepen into the role of Cav1 phosphoacceptor Y14 in caveolae assembly dynamics, we explored the oligomerization capacity of Cav1 and Cav1 Y14F in cells upon tension increase. For this we used primary *Cav1*<sup>+/+</sup> and *Cav1*<sup>Y14F/Y14F</sup> MEFs and a cross-linker agent (DSP, see methods), which allows to detect different oligomeric states of a protein<sup>99</sup>. As shown in Fig. 7g, DSP treatment provided several Cav1-immunoreactive bands which were absent in *Cav1*<sup>-/-</sup> cells (Supplementary Fig. 3k), suggesting specificity. This assay identified the following bands (from bottom to top): i) A band with an empirical size of 21.78 kDa, corresponding to Cav1 monomer, ii) a band migrating at ~44.1 kDa, which matches the expected size of two Cav1 molecules iii) a faint band of ~67 kDa, which matches the theoretical size of three Cav1 molecules (Fig. 7g). The size of these bands is incompatible with Cav1-Cavin1 complexes as the empirical size of Cavin1 in our conditions is approximately 57 kDa and the Cavin-1 showed no signal at the weight of dimer or trimer bands (Supplementary Fig. 3l). Due to size similarity, we could not determine whether Cav2 was present in those complexes, and for this reason we labeled the dimer and trimers as Cav1/2 (Fig. 7g and Supplementary Fig. 3k). Finally, we detected a smear above the dimer and around the trimers, absent in *Cav1*<sup>-/-</sup> cells, which represents Cav1 molecules in complexes of different sizes (Fig. 7g). Interestingly, hypo-osmotic shock significantly decreased the proportion of Cav1 monomers ( $p$ -value 0.002) while increasing dimers ( $p$ -value 0.009) and other oligomeric forms (trimers and larger clusters,  $p$ -value 0.013). Interestingly, the hypoosmotic-induced increase in dimer proportion was more marked in Y14F/Y14F cells ( $p$ -value for hypoosmotic: Y14F interaction 0.048), suggesting that hypoosmotic swelling alters the balance between dimers and the rest species in *Cav1*<sup>Y14F/Y14F</sup> (Fig. 7h). These results suggest that tension increase regulates the capacity of Cav1 to oligomerize and this property is partially dependent on Y14.

To gain further insight onto Cav1 molecular dynamics during adipocyte mechanoadaptation to LD growth and the relevance of Y14 phosphoregulation therein, we performed fluorescent recovery after



photobleaching (FRAP) analyses on in vitro differentiated adipocytes expressing EGFP-fusions with either wild-type Cav1 or Cav1Y14F, during normal culture or upon oleate loading. Cells expressing a wild-type Cav1-EGFP fusion showed faster fluorescent recovery upon oleate loading as compared to basal conditions (Fig. 7i). These observations suggest that caveolae flatten in response to lipid loading in differentiated adipocytes, releasing Cav1 molecules that exhibit faster dynamics (Fig. 7j). In contrast, cells expressing Cav1Y14F-EGFP displayed a distinct phenotype. In basal conditions they reached a higher fluorescent recovery as compared to Cav1WT-EGFP expressing cells

(Fig. 7i); these observations are compatible with a model whereby a minor subpopulation of Cav1Y14F molecules do not fully assemble into caveolae in basal conditions and contribute to relatively higher recovery rates (perhaps contributing to higher proportion of potential oligomeric intermediates, as observed in studies where caveolae disassembly is forced through strong hypotonic shock<sup>29</sup>; see Figs. 7g–k). However, upon oleate loading, they displayed a significantly poorer fluorescence recovery, consistent with our interpretation that caveolae from Cav1Y14F adipocytes are deficient for flattening during LD growth (Fig. 7i–k).

**Fig. 6 | Altered caveolar dynamics upon Y14F ablation. a–d** Counts for total caveolae (a), caveolae in rosettes (b), cavicles (c), and single-pits (d) in regions of increasing PM-LD distance, normalized by the perimeter comprised by those regions in the sample. Minimum cell perimeter for a cell to be included in a distance range was 5  $\mu\text{m}$ . The sample size for the five distance ranges: 18, 50, 50, 36, 23+/+ and 15, 57, 59, 36, 23 Y14F/Y14F cells. Two sample *t*-test *p* values from left to right: 0.004, 0.0009, 0.030, 0.1186, 0.6046; 0.038, 0.002, 0.113, 0.079, 0.5348; 0.106, 0.020, 0.310, 0.728, 0.997; 0.037, 0.187, 0.171, 0.773, and 0.508. **e** TIRFM Cav1-Cavin1 colocalization across indicated conditions. *P*-value for time:genotype interaction =  $4.33 \times 10^{-4}$  (*t*-test for regression coefficient). Sample size: 2097+/+ and 1994 Y14F/Y14F cells. **f** Representative images of in vitro differentiated adipocytes after 120 h of HF media. BODIPY and TIRFM images of Cavin 1 and Cav1 spots (scale bar 20  $\mu\text{m}$ ) and crops of regions central to the main adipocyte LD (scale bar 5  $\mu\text{m}$ ) are shown. **g** Caveolae circularity as a function of LD-PM proximity and genotype.

*Cav1*<sup>+/+</sup> plot was previously presented in Fig. 2c and is repeated here for clarity. *P*-value for the effect of LD-PM proximity in +/-:  $3.32 \times 10^{-10}$ ; *p*-value for proximity:genotype interaction:  $7.09 \times 10^{-6}$  (*t*-test for regression coefficient). Caveole sample size: 578 for the full range of distances, and 502 for proximity regions from 64+/+ and 69 Y14F/Y14F cells. **h, i** Schematic representation of non-circular caveolae accumulation upon LD approximation to PM. **j** Gold label counts in Y14F/Y14F samples located in caveolae, flat PM and LD surface in regions of increasing PM-LD distance, normalized by the total cellular gold label counts in the same region. **k** Gold label counts in Y14F/Y14F samples in regions of increasing PM-LD distance, normalized by the frequency of the regions in the sample. *p*-value codes: \* < 0.05, \*\* < 0.01, \*\*\* < 0.001. All boxplots show first, second and third quantiles, and whiskers extend from Q1-1.5-IQR to Q3+1.5-IQR, except in **e** where whiskers comprise the whole data range. All tests are two-sided. Source data provided as SourceData.zip.

Cav1 protein stability was not altered by Y14F mutation, neither in basal conditions of upon hypoosmotic-induced membrane tension (Supplementary Fig. 4a, b), meaning that differences in protein degradation are not likely a source for the alterations in caveolar density and response in *Cav1*<sup>Y14F/Y14F</sup> adipocytes. Collectively, these results suggest that Y14F caveolae exert partial resistance to LD-induced caveolae flattening, and thus accumulate in a deformed and compressed state (Fig. 5j) meaning that the Y14 residue is important for LD-induced caveolae mechanoadaptation.

### Y14F Cav1 mutation leads to increased adipocyte rigidity and reduced mechanical adaptation

The reduced capacity of Y14F caveolae to respond to LD expansion prompted us to measure the effects of the Y14F mutation in the mechanical properties of the tissue. Interestingly, the Y14F mutation led to increased rigidity in epididymal visceral adipose depots from animals of 45–46 weeks of age treated with HFD, although the effect was less pronounced than in Cav1-null tissues (Figs. 8a and 4e). The trend towards increased rigidity was also observed in tissues from 5 weeks-old animals treated with normal diet, albeit below statistical significance threshold (Fig. 8a). In vitro differentiated *Cav1*<sup>Y14F/Y14F</sup> adipocytes also showed increased stiffness (Fig. 8b), supporting that mechanical alterations observed in Y14F Cav1 adipose tissue samples are largely cell-intrinsic. Increased PM tension was also inferred from Flipper-TR probe fluorescence lifetime (FLT) (Fig. 8c, d). Interestingly, positive correlation of FLT with cell area in *Cav1*<sup>Y14F/Y14F</sup> adipocytes was similar to *Cav1*<sup>-/-</sup> adipocytes and opposed to *Cav1*<sup>+/+</sup> controls (Figs. 8c, d and 4h, i), suggesting that both depletion of Cav1 and its Y14 residue alter the mechanical response in the adipocyte PM. Hyperosmotic treatment reduced the probe FLT signal, supporting its correlation with PM tension (Figs. 8d and Supplementary Fig. 4c). Thus, PM tension dynamics upon adipocyte loading are also impaired in *Cav1*<sup>Y14F/Y14F</sup> adipocytes and display a behavior similar to *Cav1*<sup>-/-</sup> adipocytes.

Despite these differences in mechanical properties, *Cav1*<sup>Y14F/Y14F</sup> adipose tissue sensitivity to mechanical compression was similar to wild-type tissue (Fig. 8e, f). Thus, the mechanical effect of the *Cav1*<sup>Y14F/Y14F</sup> mutation seems to be mild, consistent with the largely preserved caveolae response (Fig. 5). Considering the fact that the deviation in caveolae disassembly in *Cav1*<sup>Y14F/Y14F</sup> adipocytes as compared to wild type cells, was more pronounced at high PM-LD proximity regions, we considered the possibility that a loading challenge was necessary to reveal a mechanical impairment in *Cav1*<sup>Y14F/Y14F</sup> adipocytes. Following this working model, we subjected adipocytes from different genotypes to a 24-hour oleate loading pulse followed by a hypoosmotic shock (Fig. 8g). Of note, *Cav1*<sup>Y14F/Y14F</sup> adipocytes showed increased fragility already in basal isosmotic, LF conditions (*p*-value 0.000, Fig. 8g and Supplementary Table 6). Oleate loading (HF) alone induced a reduction in cell viability in both *Cav1*<sup>+/+</sup> and *Cav1*<sup>Y14F/Y14F</sup> adipocytes, but there was no statistical significant difference in the response of both

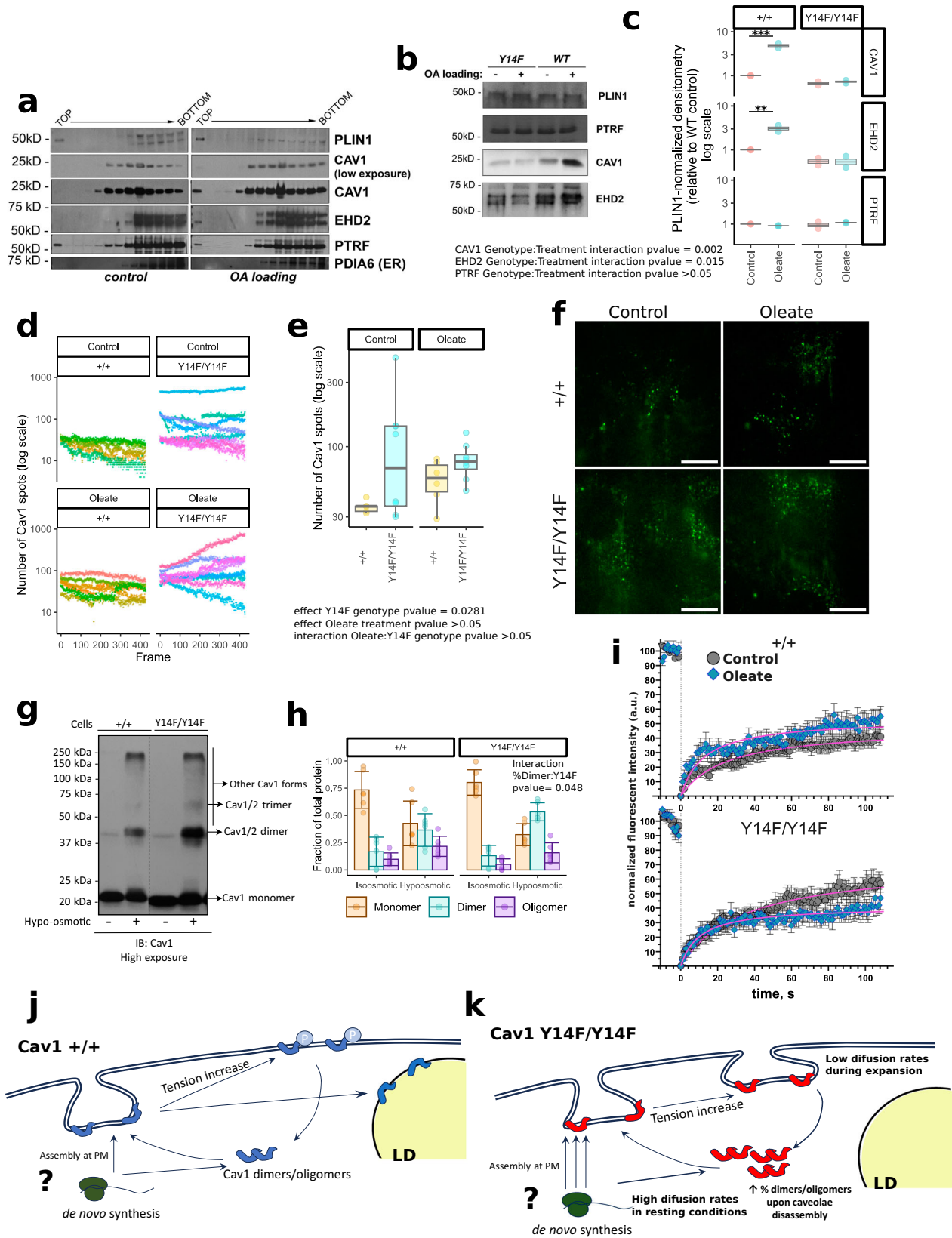
genotypes (*p*-value 0.431, Fig. 8g and Supplementary Table 6). However, addition of hypoosmotic shock rendered the interaction between genotype and oleate loading significant (*p*-value 0.034, Fig. 8g and Supplementary Table 6), supporting that hypoosmotic shock challenge after lipid loading had a more pronounced impact on *Cav1*<sup>Y14F/Y14F</sup> adipocytes as compared with wild type cells. In conclusion, *Cav1*<sup>Y14F/Y14F</sup> adipocytes were not only more fragile and susceptible to cell rupture upon usual cell culture handling (see “Materials and methods” section for details), but oleate loading significantly increased *Cav1*<sup>Y14F/Y14F</sup> adipocyte susceptibility to mechanical challenge induced by hypoosmotic shock, consistent with a model whereby adipocyte expansion reduces caveolae-dependent buffering more rapidly in mutant cells.

Of note, *Cav1*<sup>Y14F/Y14F</sup> adipocytes underwent normal morphological changes during HFD-induced adipocyte expansion, as compared to controls (Fig. 8h, i). Thus, *Cav1*<sup>Y14F/Y14F</sup> adipose tissue shows a moderate increase in rigidity and, while adipose tissue integrity is mostly preserved and its deformability is similar to controls, acute lipid loading increases susceptibility to mechanical challenge in *Cav1*<sup>Y14F/Y14F</sup> in vitro differentiated adipocytes.

### Cav1 Y14 is required for visceral adipose tissue expandability

To explore the physiological relevance of the Y14 residue in vivo, we analyzed the phenotype of *Cav1*<sup>Y14F/Y14F</sup> mice. *Cav1*<sup>Y14F/Y14F</sup> mice, similar to *Cav1*<sup>-/-</sup> mice, showed reduced body weight in normal diet (ND) as compared to control animals (Fig. 9a). Similarly, visceral depot was smaller in *Cav1*<sup>Y14F/Y14F</sup> and weighted less than control depots (Fig. 9b). This phenotype was milder as compared to *Cav1*<sup>-/-</sup> mice, which showed severely impaired expandability of adipose depots during aging, as previously reported<sup>49</sup>. In high fat diet (HFD), body weight of *Cav1*<sup>Y14F/Y14F</sup> mice was mostly preserved, although the visceral depot was also reduced as compared to controls (Fig. 9c, d). In this case, again, the phenotype was stronger in *Cav1*<sup>-/-</sup> mice (Fig. 9c, d). All these alterations were independent from body linear growth, since tibia length was similar for all genotypes (Supplementary Fig. 4d). Thus, Cav1 Y14F mutation leads to reduced adiposity.

Closer examination of *Cav1*<sup>Y14F/Y14F</sup> visceral adipose tissue showed that adipocyte average area was smaller as compared to *Cav1*<sup>+/+</sup> adipocytes—albeit larger than *Cav1*<sup>-/-</sup> adipocytes— (Fig. 9e, f), consistent with reduced depot size (Fig. 9b). However, adipocyte area increased with age, indicating that hypertrophic capacity is at least partly preserved (Fig. 9e, f). Reduced average adipocyte area was unlikely due to a shift in the distribution of adipocyte size, since median adipocyte area was identical for *Cav1*<sup>Y14F/Y14F</sup> and *Cav1*<sup>+/+</sup> animals (Supplementary Fig. 4e). However, higher area quantiles (90 and 95%) were significantly reduced in *Cav1*<sup>Y14F/Y14F</sup> (Supplementary Fig. 4f, g), suggesting specific affectation of larger adipocytes and a reduced maximum expansion threshold in the absence of Cav1 Y14 residue. Collagen deposition in *Cav1*<sup>Y14F/Y14F</sup> tissues was similar to controls (Fig. 9e), excluding the possibility that reduced adipocyte hypertrophy could be due to collagen mechanical constrictions. *Cav1*<sup>Y14F/Y14F</sup> animals



showed normal life span, as opposite to *Cav1*<sup>-/-</sup> animals, which died prematurely as previously described<sup>100</sup> (Fig. 9g).

To determine whether reduced adiposity in our models was related to differences in energy management, we measured food consumption, energy expenditure, respiratory quotient, and locomotor activity (Supplementary Fig. 4h–k and Supplementary Table 7).

We found no differences in any measured parameter between any of our models and the control. Serum profiles for different metabolic markers in *Cav1*<sup>Y14F/Y14F</sup> animals were similar to those from control mice, with normal HDL, LDL, total and free cholesterol, non-esterified fatty acids (NEFA) and triglycerides (Supplementary Fig. 5a–f). HDL, LDL, total and free cholesterol were increased for *Cav1*<sup>-/-</sup> as previously

**Fig. 7 | Cav1 Y14 phosphoacceptor regulates tension-induced Cav1 molecular dynamics.** **a** Representative WB of equal fraction volumes from sucrose gradient fractionation of homogenates from 3T3-L1 cells, subjected to indicated treatments. **b** Representative WB of LD-rich fractions purified from the indicated 3T3L1 cell line genotypes and treatments. Proteins were acetone-precipitated and 5 µg of total protein were loaded. **c** Densitometry analysis of **b** and an independent experiment. *p* values: for oleate effect in *+/+* from top to bottom: 0.0006, 0.004, 0.477; for the genotype:oleate interaction: 0.002, 0.015, 0.275. **d** Nascent EGFP-Cav1 structures detected by TIRFM after doxycycline induction across indicated conditions. One frame=840 ms. **e** Summary for time zero in **d**. *p* values: 0.028 for genotype effect, 0.252 for oleate and 0.340 for interaction, sample size from left to right: 5, 8, 6, 8 cells. **f** Representative images of nascent EGFP-Cav1 structures across indicated conditions, scale bar 20 µm. **g** Effect of osmotic swelling on Cav1 oligomeric forms in MEFs treated with DSP. Cells treated with iso-osmotic (300 mOsm) or hypo-osmotic medium (30 mOsm) for 10 min were lysed, run in non-reducing conditions

and blotted for Cav1. The specific Cav1 immunoreactive bands corresponding in size to Cav1 monomers, dimers and other oligomeric species are shown. **h** Quantitation of relative amounts of Cav1 species, as normalized to total detected Cav1 signal (*p* values for the genotype:hypoosmotic interaction: 0.186 for monomers, 0.048 for dimers, 0.841 for oligomers, *n* = 6 cell plates treated independently). Data represented as mean ±SD. **i** FRAP microscopy analyses of EGFP fusions to either Cav1 WT or Cav1 Y14F stably expressed in *Cav1*<sup>-/-</sup> fibroblasts differentiated into adipocytes. Average normalized fluorescent intensity ±SEM represented (22 control and 21 oleate treated *+/+* cells, 26 control and 17 oleate treated Y14F/Y14F cells, from two independent experiments). **j, k** Schematic depiction of models proposed for observed differences in molecular dynamics and biochemistry in Cav1 WT (**j**) and Cav1 Y14F (**k**). *p*-value codes: \*<0.05, \*\*<0.01, \*\*\*<0.001. Boxplots show first, second and third quantiles, and whiskers extend from Q1-1.5-IQR to Q3+1.5-IQR. All *p* values correspond to two-sided *t*-test for regression coefficients. Source data provided as a SourceData.zip.

reported (Supplementary Fig. 5a–d)<sup>101,102</sup>. Glucose levels in serum were similar to controls for all groups studied (Supplementary Fig. 5g), although *Cav1*<sup>Y14F/Y14F</sup> animals showed faster glucose clearance in a Glucose Tolerance Test in HFD (Supplementary Fig. 5h, i). This preservation of glucose metabolism in HFD was more evident in *Cav1*<sup>-/-</sup> animals, which in addition to faster glucose clearance showed a decreased and delayed glucose peak (Supplementary Fig. 5h–m) and a more efficient insulin response (Supplementary Fig. 5n–s).

Collectively, these results suggest that the Y14F mutation *in vivo* is sufficient to reduce caveolae sensitivity to LD growth, increase adipose tissue rigidity, and prevent physiological visceral adipose tissue expandability.

## Discussion

Hypercaloric feeding and sedentary lifestyles pose a constant challenge in adipocyte maximum expansion capacity. In conditions of overfill-derived mechanical strain, mechanoadaptation emerges as an integral aspect of adipose tissue function and homeostasis<sup>71,75,103</sup>. LD growth induces physical stress on the PM, and adipocytes become stiffer upon LD expansion<sup>103</sup>. Caveolae were reported to function as mechanosensory structures, able to flatten and provide extra membrane upon mechanical stretch to prevent cell rupture<sup>29,104</sup>. Moreover, Cav1 has been previously described as an essential protein for adipocyte expansion<sup>49</sup> and several patients with lipodystrophy due to mutations in Cav1 or PTRF have been described<sup>45–48,51–54,56,105–107</sup>.

Our study shows a clear effect of LD growth on the reorganization of the adipocyte PM. As the LD approaches the PM, the cytoplasmic space where clustered caveolae are located is reduced, increasing the pressure over the PM and caveolae. The physical and biochemical properties of caveolae favor their disassembly upon tension increase<sup>29</sup> and this could assist the accommodation of the growing LD. Indeed, our analysis revealed that LD approximation remodels PM structure, moving from complex rosette clusters to a PM with little caveolae, where single-pits predominate. Rosette density decreases in conditions of high mechanical tension<sup>35</sup> and are the caveolar structures most sensitive to mechanical stretch<sup>28,36</sup>. Consistent with these reports, we found that rosettes tend to accumulate at adipocyte regions where PM-LD distance is larger, suggesting that these structures are the first caveolae that respond to LD expansion. Also, rosette density decreased with PM-LD proximity, while the single-pit caveolae pool did not respond until PM-LD distance fell below a typical caveolar diameter. It is important to point out that we cannot rule out that single-pit caveolae do flatten upon LD proximity at long distances but are readily replaced by new single-pit caveolae coming from disassembled rosettes. Cavicles show an intermediate response as compared to single-pit caveolae and rosettes. Because our study is based on 2D sections, it is likely that most cavicles correspond to a mixture of actual rosettes and single-pits whose neck connections are not captured in 2D

acquisitions from sections. Caveolae responsiveness to LD-induced tension was also evidenced by the deformability of these structures upon LD proximity. Of note, changes in caveolar shape have been observed upon cholesterol addition<sup>108</sup>; how caveolae morphological plasticity is determined by the integration of mechanical and biochemical inputs remains an open question.

The disappearance of caveolae from the cytoplasmic space as the LD expands is compatible with a model where caveolae flatten upon LD-derived mechanical stretch to support LD expansion, providing extra membrane to compensate for increased tension and space for additional fat storage. Supporting a process of caveolae flattening, we observed increased caveolar neck width at regions of high PM-LD proximity. Caveolar membrane reservoirs would assist cell volume oscillations in fast/feeding cycles, protecting cell integrity and providing a compartment to readily store/release membrane according to the metabolic state of the adipocyte. Indeed, our estimations indicate that all caveolar membrane available in an adipocyte with small, emerging LDs, can facilitate almost a 4-fold increase in cell volume. Of note, adipocytes lacking caveolae are stiffer, less deformable and prone to mechanical rupture.

Previous reports<sup>29,36,104,109</sup> showed that Cav1 relocate to flat PM upon tension-induced caveolae flattening. However, in absolute numbers, we did not find a net increase of Cav1 in flat PM as the LD-PM distance decreased. This could be due to the slow and continuous nature of adipocyte expansion, in contrast to the acute and rapid effect of the hypoosmotic shock used in these studies<sup>29,36,104,109</sup>. It is possible that the Cav1 pool at flat PM regions diffuses to other regions or undergoes degradation, but it is constantly replaced by Cav1 from disassembling caveolae, keeping gold numbers/cell perimeter constant upon PM-LD approximation. Alternatively, Cav1 from caveolae could traffic to other regions distinct from the PM<sup>110</sup>. Indeed, parallel to caveolae disassembly, we also found that gold-labeled Cav1 at the LD surface increased with PM-LD proximity, consistent with a previous study reporting Cav1 transfer to the LD surface upon cholesterol addition, which hinted to a process of endocytosis<sup>110</sup>. Cav1 relocation to the LD upon lipid loading was also confirmed by LD fractionation experiments *in vitro*, a process that we found to be ablated by Src inhibition. Our images show a very close proximity and even an apparent contact between caveolae and the LD in regions with high PM-LD proximity, which could favor a direct transference of Cav1 to the LD, but direct evidence is lacking in this regard. Our biochemical analyses support a phosphoregulated transfer of specific caveolar components (Cav1, EHD2) but not others (Cavin1) to the LD surface upon LD expansion and approximation to the PM. This poses intriguing questions about the role of Cav1 and its potential interactors at LDs, which is currently not fully understood. Transfer of Cav1 to the LD could constitute a local signal that would inform about the expansion state of the adipocyte, as suggested for other signaling pathways<sup>111</sup>. This would provide an additional regulation layer for the integration of

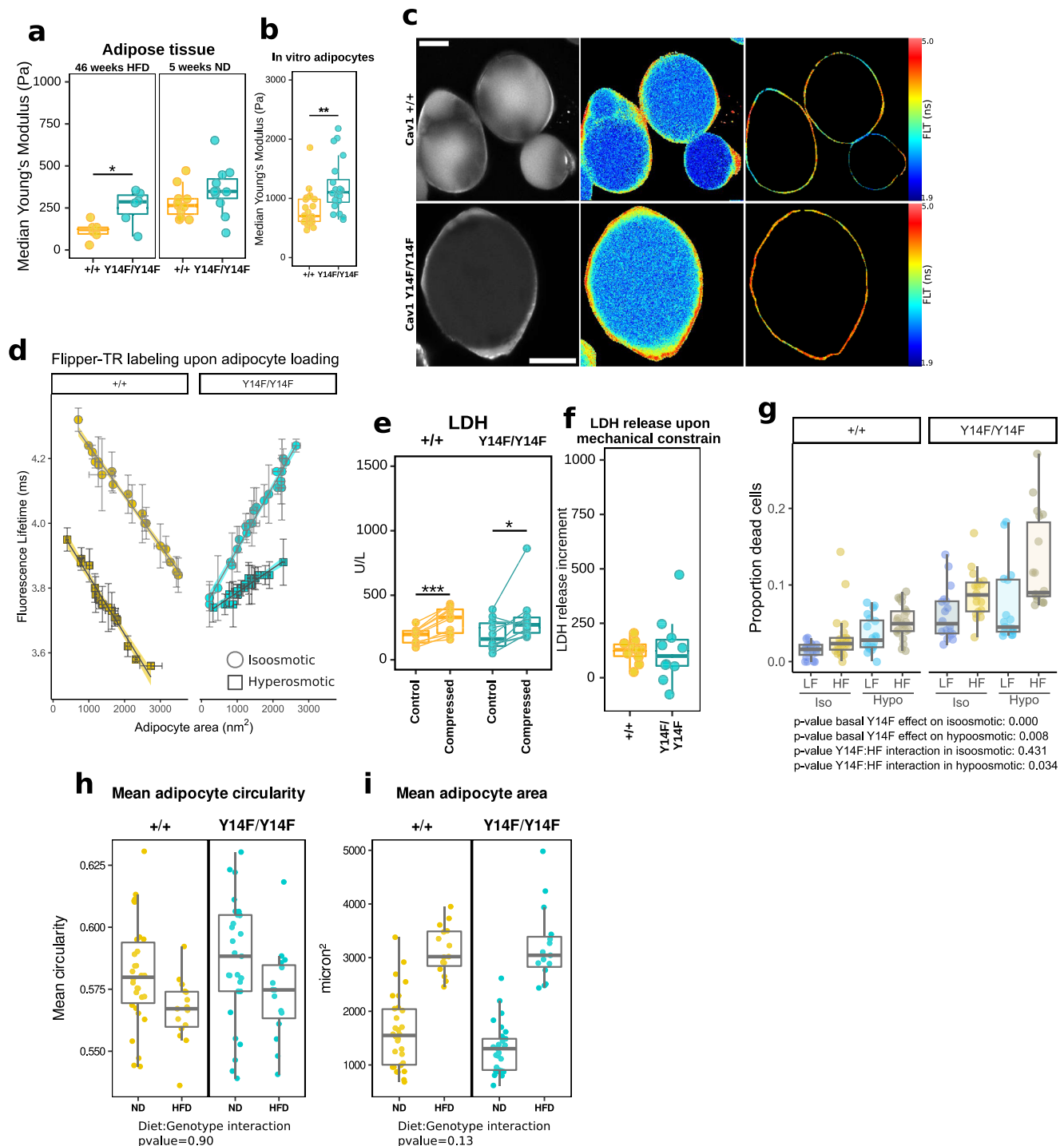
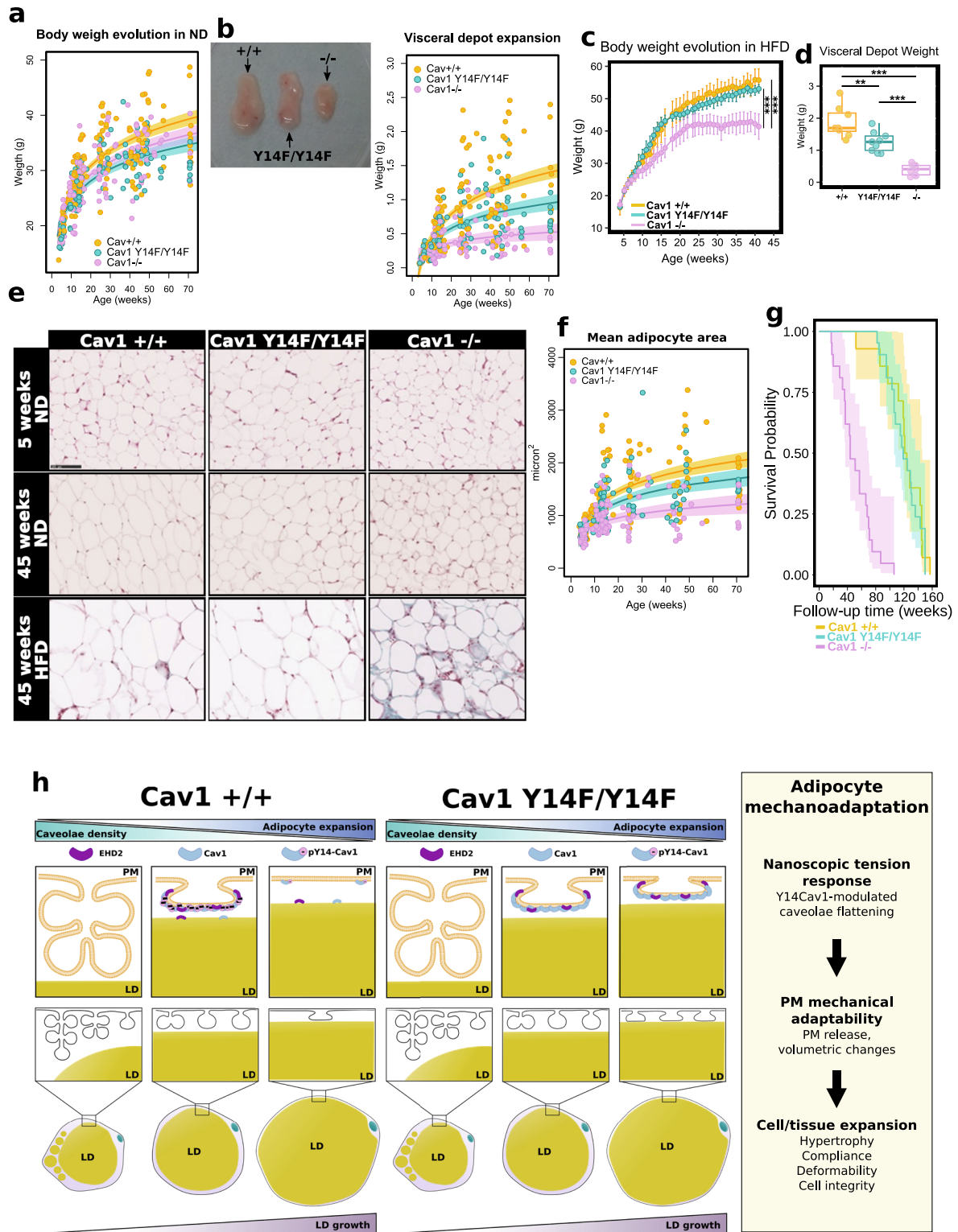


**Fig. 8 | Cav1 Y14 phosphoacceptor modulates adipose tissue mechanical properties and adipocyte mechanical response to lipid droplet expansion.**

**a** Median Young's Modulus for visceral adipose tissue explants.  $p$  values: 0.036 (HFD, 6 animals), 0.801 (ND, 11 animals). **b** Median Young's Modulus for adipocytes differentiated in vitro.  $p$  value: 0.01, 22+/+, 20 Y14F/Y14F cells from 4 animals per genotype. **c** Representative examples of Flipper-TR FLT in adipocytes after 120 h of HF treatment and their manually segmented membranes. Scale bar: 20  $\mu$ m. **d** FLT of adipocyte membrane staining of Flipper-TR as a function of adipocyte area. 24+/+, 32 Y14F/Y14F cells for iso-osmotic, 17+/+, 18 Y14F/Y14F for hyper-osmotic. Average FLT and area for different z sections  $\pm$ SEM represented. **e** LDH activity in culture media after compression. Lines connect contralateral depots of the same animal,  $p$  values:  $4.2 \times 10^{-5}$ , 0.028. **f** LDH release increment calculated as in Fig. 4c,  $p$  value = 1. Sample size for **e**, **f** 10 animals per genotype. **g** Fragility assay performed with DMEM (iso) or 1/10 DMEM dilution (hypo) on in vitro differentiated adipocytes after

incubation with 250 nM oleate (HF) or vehicle (LF). Sample size: 24 independent +/+ cell plates for HF and 20 for LF; 18 independent cell plates for Y14F/Y14F HF and LF iso and 17 for LF hypo. Effect of diet on mean adipocyte circularity (**h**) and area (**i**) in 45-week old animals.  $p$  values for the effect of diet in WT circularity and area are 0.028 and  $6.50 \times 10^{-14}$ , respectively;  $p$  values for diet-genotype interaction are 0.904 for circularity and 0.132 for area. The sample size for **h** and **i**: For ND, 30 animals +/+ and 29 Y14F/Y14F; for HFD, 15 animals per genotype. *Cav1*<sup>+/+</sup> plots and images for **a–f**, **i** where already presented in Fig. 4, and are repeated here for clarity. For **a**, **b**, **f**  $p$  values are for pairwise  $t$ -test with Bonferroni corrections, and paired  $t$ -test for **e**, all two-sided. For **g–i**  $p$ -values correspond to  $t$ -test for regression coefficients (two-sided).  $p$ -value codes: \* < 0.05, \*\* < 0.01, \*\*\* < 0.001. All boxplots show first, second and third quartiles, and whiskers extend from Q1-1.5 $\times$ IQR to Q3+1.5 $\times$ IQR. Source data provided as a SourceData.zip.



mechanical information from cell membrane onto the metabolic control of lipid traffic through the surface of the LD.

The mechanical responsiveness of Cav1 Y14 phosphorylation in vitro was previously reported for osmotic<sup>70</sup> and shear stress<sup>72</sup>; Y14 phosphorylation has also been involved in the regulation of Cav1 expression upon increased focal adhesion tension<sup>73</sup>. We have shown that Cav1 phosphorylation is also induced by lipid loading of differentiated adipocytes, and that adipocytes lacking the Y14 residue exhibit higher PM tension as they expand in size, as reported by a PM tension probe. By ultrastructure analysis, we obtained increased

caveolar density in *Cav1*<sup>Y14F/Y14F</sup> adipocytes compared to *Cav1*<sup>+/+</sup> controls. Previous studies proposed that Y14 residue is required for caveolae endocytosis<sup>38</sup>, presumably through mechanisms dependent on dynamin activity. It must be noted that these models are currently challenged, and the process of caveolae endocytosis is a subject of debate<sup>112</sup>. However, when analyzing caveolar density as a function of PM-LD distance, we found that the excess PM-associated caveolae found in *Cav1*<sup>Y14F/Y14F</sup> adipocytes was specifically associated with regions with short PM-LD distance. A shorter distance to an expanding LD implies higher PM tension, opposed to endocytosis<sup>113–115</sup>. Further, our



**Fig. 9 | Absence of Cav1 Y14 residue reduces body weight and adiposity.** **a** Body weight evolution during aging in ND. **b** Visceral depot weight during aging in ND. Representative images of three visceral depots of 47, 55, and 56 weeks of age (left to right). For A and B, sample size: 236+/+, 195 Y14F/Y14F, 196-/- animals; 95% confidence intervals shown for the estimation of the mean. **c** Body weight evolution in HFD represented by average  $\pm$  SD. Asterisks show pairwise *t*-test with Bonferroni correction for Area Under the Curve comparison, *p* value =  $6.6 \times 10^{-8}$  for +/+ vs -/-.  $5.5 \times 10^{-7}$  for Y14F/Y14F vs -/-. 0.89 for Y14F/Y14F vs +/+. Sample size: 9+/+, 10 Y14F/Y14F; 10 -/-. **d** Visceral depot weight from 45-week old animals in HFD. Sample size: 8+/+, 9 Y14F/Y14F; 9-/- animals. Pairwise *t*-test *p* values with Bonferroni correction: 0.003 for +/+ vs Y14F/Y14F comparison,  $2 \times 10^{-8}$  for +/+ vs -/-.  $6 \times 10^{-5}$  for Y14F/Y14F vs -/-. All boxplots show first, second and third quantiles, and whiskers extend from Q1-1.5-IQR to Q3+1.5-IQR. All tests are two-sided. **e** Masson's Trichrome staining

(MTS) of visceral adipose depots. Scale bar: 100  $\mu$ m. **f** Mean adipocyte area in segmented adipocytes in MTS images. Sample size: 123+/+, 102 Y14F/Y14F; 98-/- animals. 95% confidence intervals shown for the estimation of the mean. **g** Survival curve of all three genotypes. 95% confidence intervals shown. Sample size: 14 Cav1<sup>+/+</sup>, 21 Cav1<sup>Y14F/Y14F</sup> and 19 Cav1<sup>-/-</sup> animals. **h** Graphical model for caveolae response to LD expansion: LD approximates the PM during fat accumulation, inducing a transition from numerous and complex forms of caveolae (rosettes), to more sparse caveolae predominantly of the single-pit form. This process is assisted by the Cav1 phosphoacceptor Y14. The Y14 residue of Cav1 is also required for the transfer of caveolar components (Cav1, EHD2) to the LD upon expansion. The nanoscopic response of caveolae at the PM protects cell integrity and it is correlated with adipocyte mechanical adaptability to LD expansion and facilitated adipocyte hypertrophy and compliance. Source data provided as a SourceData.zip.

EM analysis did not yield any evidence for internalized caveolae structures at those regions. In addition, Cav1 relocation to the LD was preserved upon dynamin inhibition, suggesting that this process is independent from dynamin-mediated endocytosis. We interpret that increased caveolar density in Cav1<sup>Y14F/Y14F</sup> adipocytes is derived from impaired tension-driven flattening upon LD expansion. In this model, Cav1<sup>Y14F/Y14F</sup> caveolae would require closer PM-LD proximity and presumably higher PM tension to disassemble. Cav1<sup>Y14F/Y14F</sup> accumulated elongated, non-circular caveolae in regions of high PM-LD proximity, also supporting an increased number of caveolae subjected to compression but failing to flatten.

A plausible mechanism, consistent with both previous observations in vitro and our findings for caveolar morphology, would involve an alteration in caveolar curvature by the negative charges introduced by phosphorylation of Cav1<sup>74</sup>. This would facilitate caveolae unfolding, a process stalled in Y14F mutant adipocytes. The process of caveolae flattening could render the cell more compliant, since it would provide extra membrane to compensate for the applied force and, indeed, we found that adipocytes lacking caveolae are stiffer in AFM experiments. Thus, a delay in caveolae flattening could explain the moderate increase in stiffness found in non-phosphorylatable mutants. Other curvature generating molecules, such as FBP17, are also regulated by tyrosine phosphorylation<sup>36</sup> which reduces their curvature-generating capability in response to increased tension. We found a moderate expansion impairment in Cav1<sup>Y14F/Y14F</sup> visceral adipose depots, with reduced average area of Cav1<sup>Y14F/Y14F</sup> adipocytes. Thus, Y14 regulates optimal caveolae function with significant physiopathological consequences. Our biochemical and FRAP observations also support differential molecular dynamics of Cav1Y14F protein as compared to those displayed by the wild-type protein. Together with apparent differences in oligomerization dynamics upon forced caveolae disassembly, our studies suggest Y14 phosphorylation modulates intrinsic aspects of Cav1 dynamic association with different cell compartments (Fig. 7j, k).

In summary, Cav1 and its Y14 residue contribute to the mechanoadaptation of adipocytes to the expanding LD, and to the mechanical plasticity of the adipocyte PM (Fig. 9h). Absence of Cav1 or its Y14 residue impairs adipose tissue expandability, a phenotype that cannot be explained by impaired lipid uptake, increased energy expenditure or fibrosis-derived mechanical constriction of adipocytes. Absence of Cav1 or its Y14 residue alters the biophysical characteristics of adipocytes by increasing tissue stiffness in a fibrosis-independent, cell intrinsic manner. These results stress the important role of caveolae as adipocyte mechanoadaptors and mechanoprotectors, and their relevance for adipose tissue function. We propose that adipocyte caveolae mechanoadaptation is an important factor contributing to the lipodystrophy phenotype derived from Cav1 depletion. Understanding the mechanisms that ensure adipocyte expansion and integrity has clear implications for the understanding of the molecular basis of metabolic disease and adipose tissue pathologies.

## Methods

### Animal models and diets

All animal experiments were approved by CNIC and Universidad Autónoma de Madrid (UAM) Ethics Committees and by the competent authorities (Comunidad de Madrid) in compliance with relevant regulations for research animal welfare. All animal models used for experiments had a C57BL/6J (JAX® Mice Strain, obtained from Charles River) genetic background. Cav1<sup>-/-</sup> model (MGI code: Cav1<sup>tm1Kur/tm1Kur</sup>) has been previously published<sup>116</sup>. All animals used were males and fed *ad libitum*. The standard animal house diet (Normal Diet) with reference LabDiet 5K67 - JI Rat & Mouse/Auto 6 F contains 16,028% of caloric intake from fat. For (HFD) treatments, Research Diets D12492 containing 60% of calories from fat was used. For all experiments involving in vitro adipogenesis, age of animals was 12–15 weeks. EM experiments were performed on animals of 40–50 weeks and experiments involving adipose tissue explants (compression) were performed on animals from 25 to 45 weeks of age. For animals involving time course measurements, age is specified for each sample in the corresponding image.

### Generation of mice expressing Y14F-Cav1

We targeted mouse embryonic stem (ES) cells to generate a Cav1 allele coding for a substitution mutant caveolin-1 protein, that lacks the phosphorylatable residue Tyr 14. In order to generate the targeting vector, a 5.1 kbp DNA fragment, containing a fragment of Cav1 5'UTR region, exon I and a part of intron I, was subcloned upstream of a PGK-neo cassette flanked by 2 loxP sites. A 3.1 kbp DNA fragment, containing a fragment of Cav1 intron I, exon II and a fragment of intron II, was subcloned downstream of the PGK-neo cassette (Fig. 5a). The ORF codon 14 TAC sequence, coding for Tyrosine and located in exon II, was replaced by mutagenesis by TTC, which encodes for Phenylalanine, a non-phosphorylatable amino acid. A Thymidine-Kinase cassette was included in the targeting vector to confer ganciclovir sensitivity to non-homologous recombinant clones.

The resulting plasmid was electroporated in ES cells (R1 clone) and recombinant clones, resistant to G418/ganciclovir, were identified by southern blot analysis. We obtained one ES positive clone out of 442 colonies tested. This positive clone was microinjected in C57BL/6J blastocysts to generate chimeras, which were crossed with C57BL/6J females. Cav1<sup>+/NeoY14F</sup> mice were obtained by germline transmission of Cav1NeoY14F targeted allele. Cav1<sup>+/NeoY14F</sup> animals were then mated to Sox2-Cre mice, expressing an early ubiquitous-Cre, in order to remove the PGK-neo cassette and to obtain Cav1<sup>+/Y14F</sup> mice. The resulting Cav1<sup>+/Y14F</sup> mice were interbred, yielding Cav1<sup>Y14F/Y14F</sup> animals.

### Determination of biochemical parameters in serum

Blood was drawn by cardiac puncture from non-fasted animals, incubated at room temperature during 15 min and centrifuged for serum separation. Biochemical parameters in serum were obtained in the Cardiovascular Physiology Service at CNIC using an automatic

biochemical analyser Dimension RxL Max (Siemens). Dimension Clinical Chemistry, version 10.5.3: 006801-RC2 was used. The complete list of detection kits and methods is detailed in Supplementary Table 8.

### Glucose and Insulin Tolerance Test

For Glucose Tolerance Test, 10% glucose (Merk 1.04074.1000) in PBS was administered by intraperitoneal injection. For Insulin Tolerance Test, Humulin® Regular Insulin Lily, 0,75 U/ml in PBS was injected by intraperitoneal injection. The volume injected for each test was equal to 1% of body weight. Glucose was measured by a cut in the tail tip each 15 min.

### Indirect calorimetry

Food intake, energy expenditure (EE), respiratory quotient (RQ) and locomotor activity (LA) were assessed using a calorimetry system (TSE LabMaster, TSE Systems, TSE LabMaster System software version 5.05) as previously described<sup>117</sup>. In short, mice were acclimated to the metabolic cages for 48 h, followed by continuous monitoring for an additional 48 h. The indirect calorimetry system recorded data on food intake, energy expenditure, locomotor activity, and respiratory gas exchange (oxygen consumption,  $vO_2$ , and carbon dioxide production,  $vCO_2$ ) at 30-min intervals. All reported results were derived from data collected during the second 48-hour period. Locomotor activity was measured by infrared sensors that detected both horizontal and vertical movements. The respiratory quotient (RQ) was determined as the ratio of  $vCO_2$  to  $vO_2$  ( $vCO_2/vO_2$ ), reflecting the predominant macronutrient being oxidized. Energy expenditure was calculated based on  $O_2$  consumption and  $CO_2$  production using the system's standard analysis software.

Food intake, energy expenditure (EE), respiratory quotient (RQ) and locomotor activity (LA) were assessed using a calorimetry system (TSE LabMaster, TSE Systems).

### Primary MEF culture

Mouse embryos were extracted at 13 days post-fertilization. Head and liver were excised, and the remaining embryos minced and incubated in trypsin (Gibco 25200) for 15 min. Digested samples were then transferred to a 150 mm plate and incubated in DMEM+10% FBS.

### 3T3-L1 genome editing and stable rescue using lentiviral vectors

3T3L1 (ATCC CL-173) cells were transduced with lentiviral particles bearing the TLCV2 CRISPR/Cas9 3rd generation system (Addgene #87630) expressing a sgRNA guide with the sequence AGTGAT-GACGCGCACACCA. After 48 h, cultures were supplemented with 3 μg/ml puromycin and induced with 1 μg/ml doxycyclin. EGFP-positive cells were single-cell sorted onto gelatin-coated 96-well plates. Thriving clones were screened by automated immunofluorescence analysis using an Opera station (PerkinElmer). *Cav1*<sup>-/-</sup> candidate clones were further validated by western blotting. A *Cav1*<sup>-/-</sup> clone was then transduced with lentiviral particles to express either wild type or Y14F Cav1 protein as described<sup>118</sup>. Briefly, 2nd generation lentiviral particles were harvested from HEK293T cells transfected with either vector pRRLCMV-Cav1WT-IRES-GFP or pRRLCMV-Cav1Y14F-IRES-GFP, and used to transduce at a MOI=10 fresh cultures of the Cav1KO clone.

### In vitro adipogenesis and lipid loading

Subcutaneous inguinal depots were obtained from 8-15-week-old animals treated with normal diet. Fat pads were digested in a 2 mg/ml collagenase (Roche REF. 10 103 578 001)+20 mg/ml fatty acid-free BSA (Sigma A7030). Stromal-vascular fraction was separated from differentiated adipocytes by centrifugation and plated. Culture media was DMEM:F12 (BE12-719F Lonza) with 8% FBS (HyClone SV30160.03), penicillin/streptomycin (Gibco L1953096) and amphotericin B (Fungizone, BioWhittaker 17-863E). Adipogenic differentiation was

performed with the following adipogenic factors added to culture media: 5 μg/ml insulin in 3 mM HCl (Sigma I5500); 25 μg/ml IBMX (Sigma I5879); 1 μg/ml dexamethasone (Sigma D4902); 0.4415 μg/ml troglitazone (Calbiochem 648,469). After 48 h, media was replaced with new differentiation media including only insulin and troglitazone. From this point, media was changed every other day adding only insulin. AFM assays were performed at 8–9 days post differentiation.

For lipid loading assays, in vitro differentiated adipocytes were treated with culture media supplemented with 2% fatty acid free BSA, 5 μg/ml insulin, 100 μM palmitate (Sigma P0500), 25 μM cholesterol (Sigma C3045) and 1 mM oleate (Sigma O7501, in 2% BSA). Controls were treated with culture media supplemented with 5 μg/ml insulin, 2% fatty acid free BSA and the same volume of vehicle as the lipid loading media. When indicated, the dynamin I/II inhibitor Dyngo-4a (Sell-eckChem) was added 6 h before termination of the experiment at 10 μM.

### Lipid uptake assays

Epididymal depots were minced in 0.5×0.5 cm pieces and attached to the bottom of petri dishes with the biocompatible glue Histoacryl® (TissueSeal). Explants were then treated with 0.5 μM BODIPY™ 558/568 C12 (ThermoFisher, D3835) in DMEM:F12 (Lonza) with penicillin/streptomycin and amphotericin B for at least 16 h. Prior to imaging, explants were fixed with 10% buffered formalin (Sigma) and washed with PBS.

### Histopathology and immunochemistry

Tissue processing, section, staining, imaging and pathological assessment was performed at the Histopathological Unit of CNIC. Tissue sections were fixed in 10% Neutral buffered formalin (HT501128, Sigma-Aldrich) for 48 h and processed by dehydrating the tissue in increasing concentrations of ethanol, cleared in xylene, embedded in paraffin wax and sectioned at a thickness of 4 microns. For immunohistochemical analyses, sections were deparaffinized and antigen unmasking was performed using heat induced epitope retrieval (HIER) with Citrate buffer (pH6). Endogenous peroxidase was blocked by incubation with  $H_2O_2$  for 5 min and endogenous antigens blocked with fetal bovine serum (FBS) for 20 min, before incubating with the primary antibody (rabbit monoclonal anti-Caveolin 1 XP, Cell Signalling DH6G3, 1:200 dilution). As secondary antibodies, we used an HRP-conjugated goat anti-rabbit polymer (EnVision® K4003, Dako). DAB (3,3'-diaminobenzidine) was used for visualization and nuclei were counterstained with Hematoxylin. All immunohistochemical procedures were performed using an automated autostainer (Autostainer Plus®, Dako). Images were acquired with a scanner (NanoZoomer-2.0RS®, Hamamatsu).

### Histological Image Analysis

Adipocyte segmentation and quantification of adipocyte area and circularity was performed on Mason's Trichromic-stained samples, using a customized tool based on "MRI Adipocytes Tools" ImageJ macro<sup>119</sup>, developed in Fiji (ImageJ 1.51e x64)<sup>120</sup> and Matlab R2018b. Morpholib<sup>121</sup> library was used to perform mathematical morphology operations, filterings, reconstructions, and segmentations.

A first region of interest (ROI) is generated from the tissue segmentation excluding blood, fibrotic, and muscular areas detected using the different color channels. Boundaries between objects detected with Sobel edge detector<sup>122</sup> are used to extract a first segmentation of objects inside the ROI. Marker-controlled watershed algorithm<sup>123</sup> performs the adipocyte segmentation in two rounds. First, watershed driven by an initial selection of seed points (obtained from a threshold over the image) extracts adipocytes with typical size and shapes. A second marker-driver watershed, guided from a more restrictive threshold, segments smaller adipocytes in areas not covered by the first adipocyte segmentation. Area and circularity, defined

as:

$$\left(4\pi \frac{\text{area}}{\text{perimeter}^2}\right)$$

are measured for each segmented adipocyte. Additionally, percentage of fibrotic area is computed, and adipocytes are classified according to presence or absence of fibrosis in their surroundings.

### p-Y14 stimulation

A pervanadate mixture ( $\text{Na}_3\text{O}_4\text{V}$  (Sigma S6508) 0.4 M,  $\text{H}_2\text{O}_2$  3% (Sigma H1009)) was incubated during 5 min at room temperature, until it acquired a yellow-brownish color and then added in a 1/410 dilution to visceral epididymal depots, leaving the contralateral tissue as control. Tissues were minced for better surface contact and then incubated for 1 h at 4 °C in a tube rotator. After stimulation, tissues were lysed for protein extraction.

### Protein extraction, SDS-PAGE, and western blot

Protein extraction was performed with RIPA buffer (Tris-HCl 50 mM, pH 7.5; NaCl 150 mM; Triton x100 1%; SDS 0.1%; Na-deoxycholate 1%) supplemented with phosphatase and protease inhibitors (1 mM  $\text{Na}_3\text{O}_4\text{V}$ , NaF 25 mM, Aprotinin 10 µg/ml, Leupeptin 10 µg/ml, 1 mM PMSF). Tissues were lysed using a tissue lyser (TissueLyser II, Qiagen). Lysates were centrifuged to eliminate cell debris and total protein concentration was quantified using the Bradford method. 20 µg of protein were boiled and run in 15% SDS-PAGE gels and transferred to nitrocellulose membranes. Membranes were blocked with 4% BSA and immunodetection was performed with mouse anti-pCav1 (BD Biosciences clone 56 611339, lot number 43918, dilution 1:1000), rabbit anti Cav1 XP (Cell Signalling clone D46G3 3267S, lot number 8, dilution 1:1000), rabbit anti Cavin1 (Abcam, ab48824, lot number GR3178086-6, dilution 1:500) or rabbit anti EHD2 (proteintech 11440-1-AP, lot number 44-161-2324577, dilution 1:1000). Odyssey v3.0 was used for blot membrane scanning.

### Immunoprecipitation

300–600 µg of protein were immunoprecipitated from whole lysates incubating with rabbit anti Cav1 XP (Cell Signalling clone D46G3 3267S, lot number 8, dilution 1:200) for 2 h at 4 °C. 1.45 µl of antibody were used per mg of lysate. Samples were then incubated for 2 h at 4 °C with protein A (17078001, Amersham Biosciences) and washed 5 times with RIPA supplemented with protease and phosphatase inhibitors. Samples were then boiled for 5 min at 95 °C and processed for western blotting as described above.

### Atomic Force Microscopy

AFM experiments were performed by using a commercial instrument (JPK Nanowizard 3, JPK Instrument, Germany), mounted on an Axio Observer A1 inverted microscope (Carl Zeiss, Oberkochen, Germany). Tissue was minced in portions of 0.5 × 0.5 cm approximately, and attached to the bottom of petri dishes using Histoacryl® (TissueSeal). Custom AFM tips were fabricated using 50-µm-diameter polystyrene spheres (microParticles GmbH, Germany) glued to tipless cantilevers (ARROW TL1 Au, NanoWorld Arrow™, Swiss) with a nominal spring constant of 0.03 N/m. The attachment of the sphere was performed using a UV adhesive (Edmund Optics GmbH, Karlsruhe, Germany). For adipocytes cultured in vitro, a commercial cantilever with a sphere of 6.62 µm-diameter and a spring constant of 0.08 N/m were used. The cells selected to be measured accomplish an optical criteria based on its shape and size. To determine the mechanical properties of adipose tissue and adipocytes, an experimental procedure based in sequences of Force-Distance Curves (FDC) was followed. The FDCs were characterized by the application of triangular waveform movement to the AFM tip (constant tip's velocity). For tissues, tip velocity was 5 µm/s

and the maximum applied force was 15 nN. In each individual tissue, a series of 100 FDCs was performed on four different regions. These regions were separated several hundreds of microns from each other. In summary, a set of 400 FDCs were obtained for each tissue/animal. For adipocytes, tip velocity was 2 µm/s and the maximum applied force was 3 nN. In each individual cell, a series of 136 FDCs was performed. The FDCs were distributed in a grid of 8 × 8 pixels located in an area of 30 × 30 µm. This area was aligned with the center of the cell, as inferred by optical identification. To obtain the stiffness of the samples (*E*) from the FDCs, the approach part of the cycle was fitted to the Hertz model. The substrate effect induced to the *E* values obtained in the adipocytes cultured in vitro has been subtracted. To compare, together, the *E* values obtained among genotypes for cell and tissues, it is important to mention the effect of the substrate on the mechanical properties of in vitro cultured cells. Even after applying a bottom effect correction to AFM measurements, there are intrinsic phenomena that affect the mechanical behavior of the cells and, in particular, modifications of the cellular morphology and the cytoskeletal structure. These modifications are the cause originating a shift to higher *E* values for the in vitro adipocytes with respect of the tissues. However, the trend obtained among genotypes is independent of this cultured substrate effect.

### Mechanic stimulation by compression

Epididymal depots were obtained from >25 week-old animals, washed with PBS and attached to the bottom of plastic petri dishes using Histoacryl®. 50 g weights were then placed on top of fat depots and 1 ml of phenol red-free Optimum (ThermoFisher, 11058021) 1% BSA was added. Samples were incubated 4 h at 37 °C and 5% CO<sub>2</sub> and media assessed for Lactate Dehydrogenase (LDH), using an automatic biochemical analyser Dimension RxL Max (Siemens) and the detection kit DF54, Siemens.

### In vitro fragility assay

In vitro differentiated adipocytes were loaded with 250 nM sodium oleate for 24 h, washed twice with PBS 1×, and treated with diluted DMEM (1:10 in MilliQ water). After 1 min, hypo-osmotic medium was removed, and cells were trypsinized, centrifuged, stained with Trypan Blue (Sigma) and counted in a Neubauer chamber.

### Immunostaining

In vitro differentiated adipocytes were fixed with 4% formaldehyde for 15–20 min and washed with PBS. They were then incubated in blocking buffer (0.1% saponin, 0.2% BSA in PBS) and then with a 1:400 dilution of rabbit anti Cav1 XP (Cell Signalling clone D46G3 3267S, lot number 8) followed by 1:500 anti rabbit Alexa Fluor 594 (Molecular Probes, A11012, lot number 1678831). BODIPY 493/503 (ThermoFisher D3922) was then added 1:5000 for 15 min. When Cav1 and Cavin1 were costained, the antibodies mouse anti Cav1 from Sigma (SAB4200216, lot number 036M4873V) and rabbit anti Cavin1 from Abcam (ab48824, lot number GR3178086-6) were used at 1:200 dilution, and 1:500 anti mouse Alexa Fluor 647 (Molecular Probes, A11012, lot number 2300995) as secondary in addition to the previously mentioned Alexa Fluor 594.

### Microscopy Image Acquisition

Adipose tissue explants from lipid uptake assays were imaged in a Zeiss LSM 780 Upright confocal system (Carl Zeiss, Germany) with a W Plan-Apochromat 20x NA 1.0 dipping objective (REF 421452-9800) and using a high power diode (DPSS) 561 nm laser at a 20% transmission as excitation source for BODIPY C<sub>12</sub>. ZEN 2011 SP7 (black edition) 64bits version 14.0.0.201 was used. z-slices were taken every 25 microns and a maximum projection was computed for analysis.

In vitro differentiated adipocytes were imaged in a Nikon A1R confocal system (Nikon Corporation, Japan) with an objective Plan Apo VC 20x NA 0.75 dry (REF MRD00205). Samples were visualized with an

argon ion Laser 488 nm (for BODIPY 493/503) and a high-power diode 561 nm (for Caveolin-1). Nikon confocal A1R: NIS Elements AR 4.30.02. Build 1053 LO, 64 bits, was used for image acquisition.

Cav1 positive vesicles and BODIPY 493/503-positive Lipid Droplets were imaged in vitro differentiated adipocytes with a Leica AM TIRF MC (Leica Microsystems GmbH, Germany) and a HCX PL APO 100x NA 1.46 oil objective (ref 11506249). Laser Diodes Line 564 nm was used as excitation source for the visualization of Cav1 vesicles by TIRF, and Intensilight fluorescence lamp for the visualization of BODIPY. LAS-AF 2.6.0. build 7266 was used for TIRFM image acquisition.

### TIRF microscopy image analysis

Cells were manually segmented using the Cav1 epifluorescence channel and cellular fluorescence was measured in each channel. ImageJ tool “find maxima” was used to identify and count Cav1 positive spots in the TIRFM channel. Finally, the biggest LD were manually drawn, and the area recorded. If all LDs had similar size, one LD was randomly chosen and measured. The ImageJ macro TIRFvesicles.ijm was used for this procedure. Image analysis was performed with ImageJ version 1.52 h and 1.54 f.

For Cav1-Cavin1 colocalization analysis, Cav1 and Cavin1 spots were detected as previously described with the “find maxima” ImageJ tool. Coordinates of Cav1 and Cavin1 detected spots were compared and a Cav1 spot was considered to colocalized with Cavin1 when there was at least one Cavin1 vesicle within a 200 nm distance.

ImageJ macros and R scripts relevant for the analysis can be found in the GitHub repository <https://github.com/MariaAboy/AdipocyteCaveolae>.

### Transmission Electron Microscopy

For ultrastructure imaging, epididymal adipose depots were immersed immediately after extraction in fixative solution: 2% glutaraldehyde (G011 TAAB), 2% formaldehyde (28908, Thermo) in phosphate buffer 0.1 M, pH 7.4 and minced in small pieces to favor surface contact. Samples were fixed overnight, washed and treated with osmium tetroxide 1% in water; in block contrast with 0.5% uranyl in water; dehydration with increasing ethanol concentrations (30, 50, 70, 95, 100%); acetone wash and inclusion in epoxy resin Durcupan. Ultramicrotomy sections were performed with a thickness of 60 nm and then placed in copper grids and stained with uranyl acetate (2%) and Reynolds lead. Images for ultrastructure were obtained in a JEOL JEM1010 (100 kV) equipped with a digital camera Gatan Orius 200 SC with a magnification of 60000x. For immunogold imaging, epididymal adipose depots were immersed immediately after extraction in fixative solution (0.25% glutaraldehyde, 2% formaldehyde in phosphate buffer 0.1 M, pH 7.4) and minced in small pieces to favor surface contact. Samples were fixed overnight, after fixation, samples were washed twice with phosphate buffer 0.1 M, pH 7.4. and dehydrated in increasing concentrations of aqueous ethanol solution (40%, 60%, 80% and three steps of 100%). Samples were then included in LR White resin, following increasing concentrations of resin-ethanol (1:2, 1:1, 2:1, 4:1 and pure resin). Samples were placed in individual capsules avoiding air bubbles. Samples were left in a heater at 50 °C during three days for resin polymerization. For immunogold labeling, 70–80 mm thick LR White sections were incubated with 50 nM NH<sub>4</sub>Cl for 10 min to quench the free aldehyde groups and with 10% FBS for 10 min to block nonspecific binding. Then, primary rabbit Cav1 XP (Cell Signalling clone D46G3 3267S, lot number 8) antibody was incubated for 1 h at RT (1/10 dilution), followed by addition of protein A conjugated to 10-nm gold particles (EM Laboratory) for 45 min at RT. Sections were stained with uranyl acetate and lead citrate before visualization. Samples were imaged with a JEM1400 Flash (Jeol) with a camera CMOS Oneview (Gatan), with a ×150,00 magnification. Gatan Microscopy Suite, DigitalMicrograph version 2.30.542.0 (1996–2013 Gatan Inc.) was used for EM image acquisition.

### TEM image analysis

Ultrastructure image tiles were manually reconstructed and stitched with the MosaicJ plugin<sup>124</sup> and the Grid Collection Stitching plugin<sup>125</sup> in ImageJ<sup>120</sup>. Caveolae were then manually located, counted and classified with the Cell Counter plugin<sup>126</sup>. Caveolae were classified in three groups: the “single-pit” group, which included all individual caveolae connected by a neck to the PM; the “rosettes” group, which included all caveolae grouped in clusters or rosettes and from which we counted individually each one of the invaginations that formed the cluster; and the “cavicles” group, which included all caveolae that were apparently disconnected from the PM or caveolae clusters. Previous work showed that rosettes and cavicles are, in the vast majority of the cases, connected with the plasma membrane despite their apparent detachment. Cavicles and rosettes that frequently appear to be PM disconnected, are actually connected to the PM, as shown before<sup>36,37,77,78</sup>; although a small fraction of them could represent in transit caveolar carriers<sup>51,127</sup>. PM and LD of each cell were manually drawn and the perimeter length measured. Cytoplasmic pixel coordinates in the space between PM and LD were obtained for further image processing in R<sup>128</sup>.

In order to facilitate further computational analysis, the cell was tessellated applying a square grid of 20×20 pixels (29.6×29.6 nm). Caveolae coordinates that were manually determined were projected to the closer grid points. Finally, the minimum distance of each grid point to the PM and the LD was calculated using the euclidean distance. The PM-LD distance through every grid point was calculated by adding PM-grid + grid-LD distance. Median PM-LD distance of a cell was calculated as the median of the PM-LD distance of all the grids in the cell. Through-caveolae PM-LD distance was calculated as the PM-LD distance of the grid point closer to the manually assigned caveolae coordinate. As the grid size was 20×20 pixels, caveolae coordinate to grid projection has a maximum error of 14.14 pixels (21 nm) with respect to the manual location of caveolae, which corresponds with half a diameter of a 20×20 pixel square. R script “TEMscript.R” was used for this process.

In order to determine the membrane perimeter covered by regions of different PM-LD distance, the macro CompleteCaveolaeAnalysis.ijm was used to 1) obtain the euclidean distance between Plasma Membrane (PM) and Lipid Droplet (LD) coordinates once every 8 pixels of PM, and 2) calculate the PM-LD distance through each caveolae coordinate. Image analysis was performed with ImageJ version 1.52 h and 1.54 f.

Samples from a total of 4 *Cav1*<sup>+/+</sup> and 4 *Cav1*<sup>Y14F/Y14F</sup> animals were prepared, providing sections from 64 *Cav1*<sup>+/+</sup> and 69 *Cav1*<sup>Y14F/Y14F</sup> adipocytes. 22077 caveolae were counted for *Cav1*<sup>+/+</sup> and 28177 for *Cav1*<sup>Y14F/Y14F</sup>, along a total perimeter of 5366.186 microns for *Cav1*<sup>+/+</sup> and 6126.138 microns for *Cav1*<sup>Y14F/Y14F</sup>. 1085 caveolae were randomly selected for manual shape analysis using the ImageJ polygon tool, 578 for the full range of distances, and 502 for proximity regions.

Immunogold images were similarly reconstructed and stitched. Caveolae and golds were counted and classified with the multi-point tool of ImageJ. Caveolae were classified in three categories previously defined: “single-pit”, “rosette”, “cavicle”. Golds were classified as “gold in single-pit”, “gold in rosette” or “gold in cavicle” if they were located in caveolae; “gold in flat membrane” if located in PM with no caveolar structures; “gold in LD membrane” if located close to the LD membrane, with no nearby caveolar structures; “gold elsewhere” if they were located in the cytoplasm, with no clear adjacent caveolar structure; “gold outside” when located outside cell bounds or within LD but far from the LD membrane. Since the LD stores only lipids and should be devoid of material after sample processing, it should correspond to an empty space and golds inside the LD should be considered background. PM-LD distances, distances through caveolae and golds and cell perimeter were calculated following the method previously described for ultrastructural analysis. R script “IGscript.R” was used for this process. Samples from 1 *Cav1*<sup>+/+</sup>, 1 *Cav1*<sup>Y14F/Y14F</sup> and 1 *Cav1*<sup>-/-</sup> animals

were prepared, providing sections for 31 *Cav1*<sup>+/+</sup>, 28 *Cav1*<sup>Y14F/Y14F</sup> and 13 *Cav1*<sup>-/-</sup> cells. 10523 *Cav1*<sup>+/+</sup>, 17552 *Cav1*<sup>Y14F/Y14F</sup> and 155 *Cav1*<sup>-/-</sup> structures with caveolar morphology were counted. 7730 golds for *Cav1*<sup>+/+</sup>, 9404 golds for *Cav1*<sup>Y14F/Y14F</sup> and 2138 golds for *Cav1*<sup>-/-</sup> samples were counted. Total analyzed cell perimeter was 3300.882 microns for *Cav1*<sup>+/+</sup>, 3690.73 microns for *Cav1*<sup>Y14F/Y14F</sup> and 1951.738 microns for *Cav1*<sup>-/-</sup> samples. Virtual absence of gold-labeled or unlabeled caveolar structures in *Cav1*<sup>-/-</sup> samples confirmed the specificity of caveolae staining and identification (Supplementary Fig. 6a-h). Gold labels at flat PM and LD were clearly decreased in *Cav1*<sup>-/-</sup> samples while staining outside the cell (i.e. unspecific background) was similar across genotypes (Supplementary Fig. 6i-l). While the “elsewhere” category was clearly increased in *Cav1*<sup>+/+</sup> and *Cav1*<sup>Y14F/Y14F</sup>, we found significant amounts in *Cav1*<sup>-/-</sup> adipocytes, indicating that a significant amount of gold labels in this group were unspecific. We thus excluded this category from our analysis. Staining efficiency was estimated as 15–20% upon computing the fraction of gold-labeled-positive caveolae (Supplementary Fig. 6m-p). To assess object (caveolae or gold) numbers in *Cav1*<sup>+/+</sup> and *Cav1*<sup>Y14F/Y14F</sup> genotypes, we produced normalized histograms of object counts through PM-LD regions. In order to do this, we distributed the distance data in bins and obtained the frequencies (i.e. counts of caveolae or golds) for each bin. We then divided this frequency by the frequency of those distances in the whole sample (counts of grids with that PM-LD distance).

### Two-photon Fluorescence Lifetime Imaging Microscopy

We obtained in vitro differentiated adipocytes and at day 8 of differentiation we treated them with DMEM:F12 media 8% FBS supplemented with 2% fatty acid free BSA, 5 µg/ml insulin, 100 µM palmitate (Sigma P0500), 25 µM cholesterol (Sigma C3045) and 1mM oleate (Sigma O7501, in 2% BSA) for 120 h. On the acquisition day, we incubated the cells with Flipper-TR (810250 C, Avanti® Polar Lipids, Inc) during 30 min and washed. The fluorescence lifetime of Flipper changes according to different environments and stiffness of the membrane cell: it becomes longer when it is closely packed into the bilayers of the plasma membrane; it decreases when Flipper molecules are in less compacted areas. Fluorescence lifetime was acquired by an inverted Nikon Eclipse Ti microscope, using a Plan Apo VC 60× A/1.20 WI water immersion objective (Nikon, Corp.). Two-photon excitation was obtained using a tunable Spectra Physics femtosecond laser, model Mai Tai DeepSee, coupled to an acousto-optic pulse picking modulator and detected with an Alba imaging workstation (ISS, Inc.). Flipper-TR dye treated cells were excited at 900 nm with laser power of between 0.75 and 1.84 mW at the sample and the emission was collected with a 530/43 nm bandpass filter. Fluorescence Lifetime Imaging Microscopy (FLIM) was performed on the ISS Alba 5 multiphoton imaging system (ISS, Inc., Champaign, Illinois, USA) using the FastFLIM, which is implemented by the digital frequency domain method (Colyer et al.). Data were acquired and processed by VistaVision\_x64\_V4.2\_Build 373 software (ISS, Inc., Champaign, Illinois, USA). The scan area (256×256 pixels), acquired with a pixel dwell time of 64 µs, was in the range between 30 × 30 µm<sup>2</sup> to 110 × 110 µm<sup>2</sup>, with a pixel size between 117 nm to 429 nm, and a voxel size between 0.117×0.117×1.000 µm<sup>3</sup> to 0.429×0.429×1.000 µm<sup>3</sup> (X,Y,Z). Before sample measurements, a concentrated fluorescein solution at pH 9.5 was measured and used as fluorescence lifetime calibration. Fluorescein lifetime (4.04 ns) was determined separately in a fluorometer (PC1; ISS, Inc., Champaign, Illinois, USA).

Procedure for FLIM analysis: the membrane of each adipocyte was manually segmented in ImageJ, where adipocyte area was also obtained. Fluorescence lifetime decays were analyzed by the phasor-FLIM method using phasor analysis module of VistaVision\_x64\_V4.2\_Build 373 software (ISS, Inc., Champaign, Illinois, USA), limited to the segmented membrane area. The distribution was obtained by converting the multiexponential fluorescence decays

acquired in each pixel into the graphical representation of a phasor. In brief, the phasor transformation does not assume any fitting model for fluorescence lifetime decays. It simply expresses the overall decay in each pixel in terms of a vector of (s, g) polar coordinates in the so-called “universal circle”<sup>129</sup>.

### Total internal reflection fluorescent microscopy assessment of de novo Cav1 cluster formation

Analysis of de novo formation of CavWT-GFP or Cav1Y14F-GFP clusters was performed as previously described<sup>130</sup>. TIRF microscopy was performed with a Leica AM TIRF MC microscope. TIRFm movies were acquired with a 100× 1.46 NA oil-immersion objective at 488 nm excitation and an evanescent field with a nominal penetration depth of 150 nm. Images were collected with an ANDOR iXon CCD at 840 ms per frame. For density analysis, particles were analyzed by finding and counting local maxima using LoG 3D plugin<sup>131</sup> (ImageJ). Either *Cav1*<sup>+/+</sup> or *Cav1*<sup>Y14F/Y14F</sup> were subcloned in doxycycline inducible TLCV2 plasmid substituting Cas9 to obtain GFP fusion proteins. *Cav1*<sup>-/-</sup> fibroblasts were electroporated with TLCV2 *Cav1*<sup>+/+</sup> GFP or TLCV2 *Cav1*<sup>Y14F/Y14F</sup> GFP plasmids. Positive clones were selected by culturing cells in puromycin containing DMEM throughout experiments. We titrated doxycycline and found a specific dose able to induce protein expression 5 min prior to imaging. Lipid loading time in this experiment was 24 h, prior to doxycycline addition, and then followed by spot imaging over an averaged period of 20 min, analyzing different cells within each plate. To estimate caveolae biogenesis in regions proximal to the LD as opposed to the rest of the cell, we performed Oil Red staining immediately after life image acquisition and acquired an additional image with the stained LDs. Next, we classified Cav1 clusters depending on their colocalization with the LDs. Clusters that were localized inside (thus below in the z-axis) the area of the LDs were assumed to colocalize. Cluster density was calculated dividing the number of Cav1 clusters inside or outside the LD region by the cell area corresponding to the LDs or the cell area excluding LDs, respectively. To perform paired statistical analysis, the difference of the cluster density inside and outside LD was calculated for each cell. LAS-AF 2.6.0. build 7266 was used for TIRFM image acquisition.

### Fluorescence recovery after photobleaching

*Cav1*<sup>-/-</sup> fibroblasts were electroporated with TLCV2 Cav1WT GFP or TLCV2 Cav1Y14F GFP plasmids. Positive clones were selected by culturing cells in puromycin-containing DMEM throughout experiments. Pre-bleached events were acquired for 10 s before bleaching by stimulation with the Nikon scanner at 488 nm. Fluorescence recovery was monitored continuously until the intensity plateaued (approximately 1.5 min). Fluorescence during recovery was normalized to the pre-bleach intensity after subtracting intensity at bleaching timepoint. Cells were cultured in DMEM (Thermo Fisher Scientific) supplemented with 10% FBS, and 1% penicillin, and streptomycin. Protein expression was induced by adding doxycycline 5 min prior to imaging.

### Oligomerization assay in cells

Cells were treated with DMSO vehicle or DSP (dithiobis[succinimidylpropionate], ThermoFisher 22585), at a final concentration of 0.5 mM for 5 min at room temperature, followed by Tris-HCl, pH 7.5 at a final concentration of 20 mM during 15 min. Cells were lysed in sample buffer without reducing agent, briefly sonicated on ice and run in a SDS-PAGE; samples were not boiled. For the calculation of the molecular weight of each band, the position of the band center was compared to the position of the labeled molecular weight markers.

### Protein stability assay

To follow the stability of the protein, protein synthesis was inhibited with cycloheximide (Sigma, O1810) and the protein levels were

determined by western blot over the period of time indicated in each experiment.

### Lipid droplet purification

LD purification was achieved by flotation through a sucrose gradient following published guidelines<sup>95</sup>. Briefly,  $10^7$  in vitro differentiated adipocytes were loaded with 250 nM sodium oleate for 24 h, rinsed in PBS, gently scrapped in 500 microlitres of hypotonic medium (10 mM TrisHCl pH 7.5, 10 mM KCl, 1 mM EDTA, and protease inhibitors), and homogenized through 10 passages through a 21 G needle. Homogenates were spun at 1600 g for 5 min and the postnuclear supernatants were mixed at 1:1 volume ratio with 2.5 M sucrose in hypotonic medium. A stepwise sucrose gradient (30, 25, 20, 15, 7.5 and 5%) of 10 ml was layered on top in ultracentrifuge tubes and centrifuged at 130000 g for 3 h on a SW40Ti rotor. Typically, 14 fractions of 70  $\mu$ l were manually harvested from top to bottom for western blotting analysis; in some cases, only 9 fractions of 1 ml were harvested. When indicated, the top LD-rich fraction was precipitated with acetone and resuspended in 10 mM TrisHCl, 2% SDS solution for precise protein concentration determination before western blotting.

### Quantification of caveolar contribution to adipocyte volumetric oscillations

Caveolar flattening provides additional membrane surface<sup>29</sup> and could thereby enable adipocyte expansion by readily increasing cellular volume. To estimate this effect, we considered the adipocyte with the largest median PM-LD distance in our dataset (1.78 microns), which had 9.13 caveolae per micron of PM perimeter. This corresponds to 83.36 caveolae per square  $\mu$ m of PM surface. Assuming a spherical morphology for caveolae and a typical value of 80 nm in diameter, the surface area for individual caveolae would correspond to  $4\pi \cdot 0.040^2 = 0.02 \mu\text{m}^2$ , and total caveolar area would be  $0.02 \cdot 83.36 = 1.67 \mu\text{m}^2$  per  $\mu\text{m}^2$  of PM. Thus, the fraction of caveolar membrane content per unit would be  $1.67 / (1.67 + 1) = 0.63$ , meaning that caveolae comprise up to 63% of total adipocyte membrane surface area. Based on our analysis of caveolae disappearance as the LD grows (Fig. 1) and previous reports<sup>28,36</sup>, about 90% of caveolae could completely flatten out. This magnitude of caveolae flattening would result in a final  $1 + 0.9 \cdot 1.67 = 2.50 \mu\text{m}^2$  per initial  $\mu\text{m}^2$  of PM, and thereby account for a 2.50x increase in cell surface, which would correspond to a  $(\sqrt{2.50}) = 3.95$ x increase in adipocyte volume.

### Calculation of area coverage percentage by circles in hexagonal packing arrangement

The maximum area covered by circles of radius  $r$  is achieved when they are arranged in a hexagonal lattice. Therefore, by computing the area of a hexagon (that tessellate the whole 2D space), and the area of the inscribed circle (Supplementary Fig. 2m), we can obtain the maximum fraction of area covered by circles as the ratio between both areas.

A hexagon would be composed by 12 triangles as shown in Supplementary Fig. 2m. From simple trigonometry calculations, we obtain the radius of the hexagon ( $L$ ):

$$L = 2 \times r \times \tan(30^\circ) = 2r \frac{\sqrt{3}}{3} \quad (1)$$

The base of the triangle would equal:

$$(2r \cdot \sqrt{3})/3/2 \quad (2)$$

Leading to a triangle area,  $A_t$ :

$$A_t = \frac{(r \cdot (2r \cdot \sqrt{3})/3)/2}{2} = \frac{\sqrt{3}}{6} r^2 \quad (3)$$

The hexagon area ( $A_h$ ) will thus result:

$$12 \times A_t = A_h = 2\sqrt{3} \cdot r^2 \quad (4)$$

The area of the inscribed circle is:

$$A_c = \pi \cdot r^2 \quad (5)$$

With this we obtain the fraction of hexagon covered by a circle:

$$(A_c/A_h) : \pi/2\sqrt{3} = 0.90689 \quad (6)$$

Thus, packing of perfect circles would cover at most approximately 90.7% of the area.

### Statistics and reproducibility

All data representation and statistical analysis was performed in RStudio Version 2023.03.0 and R 4.2.3<sup>132</sup>. Packages `lattice`<sup>133</sup>, `ggplot2`<sup>134</sup> and `beeswarm`<sup>135</sup> were used for data visualization and packages `plyr`<sup>136</sup> and `data.table`<sup>137</sup> for dataframe management. Packages `survival`<sup>138,139</sup> and `survminer`<sup>140</sup> were used for survival statistical analysis and representation. Packages `dunn.test`<sup>141</sup> and `FSA`<sup>142</sup> were used to perform Dunn's test. Longevity of animal models was assessed with Kaplan–Meier survival curves.

Correlation of quantitative variables in independent animals or cells was modeled by linear regression (serum biochemical parameters through age, energy expenditure by lean mass). To acquire linearity, we log-transformed some independent variables: age for analysis of body weight, fat depot weight, adipocyte area, tibia length; PM-LD distance for analysis of caveolae counts. To acquire linearity, we log-transformed both dependent and independent variables in the case of gold label counts in caveolae, flat PM or LD surface across PM-LD distance. When relationship between dependent and independent variables was curved (adipocyte circularity through age), and linearity could not be achieved by log-transformation, we used additive models with splines smoothing.

Correlation of quantitative and categorical variables (genotype and PM-LD proximity effect on caveolae circularity, genotype and diet effect on adipocyte area and circularity, genotype and light effect on energy expenditure, respiratory quotient and locomotor activity) was modeled by linear regression.

Repeated measures performed in the same individual at pre-established time intervals (i.e., body weight follow-up in the same mouse cohorts, glucose levels in GTT and ITT experiments) were analyzed by Area Under the Curve (AUC) method. Values for AUC were then compared across all three genotypes using one-way ANOVA with pair-wise  $t$ -test, with Bonferroni correction for multiple comparisons. Alternative hypotheses were two-sided.

For data from independent cells/animals of three or more groups, one-way ANOVA was used when data was roughly symmetrical: weight of visceral depots, AFM measurements, LDH release increment, LDH release at basal conditions, GTT and ITT parameter and 48-h food intake. Pair-wise  $t$ -test with Bonferroni correction for multiple comparisons was performed. When data was clearly not normally distributed, or equality of variances could not be assumed, Kruskal–Wallis H test was used instead, with post-hoc Dunn's test of multiple comparisons correcting  $p$ -values with the Bonferroni method: Cav1 spot intensity, bodipy intensity, LD area, and Cav1 intensity during lipid loading of in vitro differentiated adipocytes and comparison of number of caveolae and golds between three genotypes. Alternative hypotheses were two-sided.

For comparison of two groups with roughly symmetric distribution and equal variances (Bodipy C12 intensity, normalized caveolae counts), two sample  $t$  test was used. When variable distribution was clearly non-symmetric, or variances could not be assumed as equal,

Wilcoxon signed-rank test was used (caveolae morphology parameters, number of caveolae per micron of cell perimeter, percentage of fibrotic adipocytes, average PM-LD distance). Alternative hypotheses were two-sided.

For paired data, we used paired *t*-test (comparison of fibrotic and non-fibrotic adipocytes from the same animal; LDH release for contralateral depots) or Wilcoxon signed rank test for the difference between the two conditions (differences between distance through caveolae types). Alternative hypotheses were two-sided.

Caveolae and gold label density in ranges of PM-LD distance was represented using normalized histograms as detailed in the previous section. For statistical inference, we calculated a normalized caveolae counts for each cell in each distance range (for example, number of caveolae in regions of 0–100 nm, divided by the frequency of these regions in the cell), and compared both genotypes by two-sample *t*-test. A cell was included in a distance range only if these regions comprised at least 5 microns of cell perimeter.

Regular Electron Microscopy experiments (Figs. 1, 2a–g, 5d–r, 6a–d, g, Supplementary Figs. 1 and 3f) were performed twice independently, including tissues from two *Cav1*<sup>+/+</sup> and two *Cav1*<sup>Y14F/Y14F</sup> animals each time. In addition, Immunogold labeling (Figs. 2l–n, 3b, 6j, k, Supplementary Figs. 2g–i, and 6) was performed once in tissues of one animal per genotype. TIRFM experiments for *Cav1* spot detection (Figs. 2h–j, Supplementary Figs. 2c–e, and 3c) were performed twice independently obtaining similar results, and similar results were also obtained in two independent additional experiments that included Cavin1 staining for colocalization studies (Fig. 6e, f). Flipper-TR FLT experiments (Figs. 4h, i, 8c, d, Supplementary Figs. 2n–o, and 4c) were performed 5 times (three with the isosmotic protocol and two with the hyperosmotic). AFM measurements (Figs. 4d–f and 8a, b) in tissues were performed three times independently, and twice in *in vitro* differentiated adipocytes. Mechanical compression and LDH measurements (Figs. 4a–c and 8e, f) comprise 9 independent repetitions in different days. Timecourse descriptive experiments of adipocyte morphological parameters (Figs. 3a, c–i, 8h, i, 9a, b, f, Supplementary Figs. 3d, 4d–g, and 5a–g) were performed on independent animals sacrificed at the specified ages over the course of 4 years. Follow-up of mouse cohorts on HFD (Fig. 9c, d) was performed three times. Survival experiment was performed once (Fig. 9g). Metabolic cage and glucose metabolism tests were performed twice (Supplementary Figs. 4h–k and 5h–s). Western Blot analysis of *Cav1* levels and phosphorylation was performed four times (Fig. 5b, Supplementary Fig. 3a, b). Western Blots after loading and fractionation experiments were performed twice (Figs. 5c, 7a–c, and Supplementary Fig. 3e, g–i). FRAP (Fig. 7i) and *de novo* *Cav1* cluster formation experiment were performed twice (Fig. 7d–f and Supplementary Fig. 3j). *Cav1* stability (Supplementary Fig. 4a, b) and dimerization (Fig. 7g, h and Supplementary Fig. 3k, l) experiments were performed three times. Fragility assays (Fig. 8g) were performed 4 times. Hypoosmotic shock experiment was performed once (Supplementary Fig. 2f) and lipid uptake (Supplementary Fig. 2j, k) was performed 4 times, with one explant from one animal per genotype each time.

Test results were summarized in plots and tables with asterisks: one asterisk (\*) for *p*-value < 0.05; two asterisks (\*\*) for *p*-value < 0.01 and three asterisks (\*\*\*) for *p*-value < 0.001. All boxplots show first (Q1), second (median), and third (Q3) quantiles, and whiskers extend from Q1–1.5×IQR (interquartile range) to Q3+1.5×IQR. Data points farther than this distance are considered outliers and plotted as individual dots. In cases where the sample size was too big and the visualization of outliers was not informative, whiskers were extended to the full range of data, and this was stated in the figure caption.

## Reporting summary

Further information on research design is available in the Nature Portfolio Reporting Summary linked to this article.

## Data availability

Image datasets generated in this study have been deposited in zenodo: TEM images of *Cav1*<sup>+/+</sup> adipocytes [<https://doi.org/10.5281/zenodo.13835670>] TEM images of *Cav1*<sup>Y14F/Y14F</sup> adipocytes [<https://doi.org/10.5281/zenodo.13860168>] immunogold of *Cav1*<sup>+/+</sup> adipocytes [<https://doi.org/10.5281/zenodo.13880307>] immunogold of *Cav1*<sup>Y14F/Y14F</sup> adipocytes [<https://doi.org/10.5281/zenodo.13880329>] immunogold of *Cav1*<sup>+/+</sup> adipocytes [<https://doi.org/10.5281/zenodo.13880353>] TIRF images from *Cav1*<sup>+/+</sup> adipocytes [<https://doi.org/10.5281/zenodo.13880363>] TIRF images from *Cav1*<sup>Y14F/Y14F</sup> adipocytes [<https://doi.org/10.5281/zenodo.13880372>] All processed data are provided in the Source Data file SourceData.zip, and are also available on zenodo: - <https://doi.org/10.5281/zenodo.13881240> Source data are provided with this paper.

## Code availability

Custom R scripts and ImageJ macros can be found at <https://github.com/MariaAboy/AdipocyteCaveolae> (<https://doi.org/10.5281/zenodo.1390222>).

## References

1. Tan, C. Y. & Vidal-Puig, A. *Biochemical Society Transactions*. Vol. 36. p. 935–940 (Portland Press, 2008).
2. Vishvanath, L. & Gupta, R. K. Contribution of adipogenesis to healthy adipose tissue expansion in obesity. *J. Clin. Investig.* **129**, 4022–4031 (2019).
3. Rajala, M. W. & Scherer, P. E. Minireview: the adipocyte - At the crossroads of energy homeostasis, inflammation, and atherosclerosis. *Endocrinology* **144**, 3765–3773 (2003).
4. Moreno-Indias, I. & Tinahones, F. J. Impaired adipose tissue expandability and lipogenic capacities as ones of the main causes of metabolic disorders. *J. Diabetes Res.* **2015**, 970375 (2015).
5. Eliasson, B. et al. Amelioration of insulin resistance by rosiglitazone is associated with increased adipose cell size in obese type 2 diabetic patients. *Adipocyte* **3**, 314–321 (2014).
6. Parlee, S. D., Lentz, S. I., Mori, H. & MacDougald, O. A. *Methods in Enzymology*. Vol. 537. p. 93–122 (Academic Press Inc., 2014).
7. Huang-Doran, I., Sleight, A., Rochford, J. J., O'Rahilly, S. & Savage, D. B. Lipodystrophy: metabolic insights from a rare disorder. *J. Endocrinol.* **207**, 245–255 (2010).
8. Robbins, A. L. & Savage, D. B. The genetics of lipid storage and human lipodystrophies. *Trends Mol. Med.* **21**, 433–438 (2015).
9. Garg, A. & Agarwal, A. K. Lipodystrophies: disorders of adipose tissue biology. *Biochim. Biophys. Acta Mol. Cell Biol. Lipids* **1791**, 507–513 (2009).
10. Garg, A. Lipodystrophies: genetic and acquired body fat disorders. *J. Clin. Endocrinol. Metab.* **96**, 3313–3325 (2011).
11. van der Pol, R. J. et al. Berardinelli-Seip syndrome and achalasia: a shared pathomechanism? *Eur. J. Pediatr.* **174**, 975–980 (2015).
12. Hussain, I. & Garg, A. Lipodystrophy syndromes. *Endocrinol. Metab. Clin. North Am.* **45**, 783–797 (2016).
13. Wang, M. Y. et al. Adipogenic capacity and the susceptibility to type 2 diabetes and metabolic syndrome. *Proc. Natl Acad. Sci. USA* **105**, 6139–6144 (2008).
14. Hammarstedt, A., Gogg, S., Hedjazifar, S., Nerstedt, A. & Smith, U. Impaired adipogenesis and dysfunctional adipose tissue in human hypertrophic obesity. *Physiol. Rev.* **98**, 1911–1941 (2018).
15. Khan, T. et al. Metabolic dysregulation and adipose tissue fibrosis: role of collagen VI. *Mol. Cell Biol.* **29**, 1575–1591 (2009).
16. Yamada, K. Some aspects of the fine structure of the gall bladder epithelium of the mouse. *Okajimas Folia Anat. Jpn* **45**, 11–19 (1968).
17. Farquhar, M. G. & Palade, G. E. Junctional complexes in various epithelia. *J. Cell Biol.* **17**, 375–412 (1963).
18. Meshulam, T., Breen, M. R., Liu, L., Parton, R. G. & Pilch, P. F. Caveolins/caveolae protect adipocytes from fatty acid-mediated lipotoxicity. *J. Lipid Res.* **52**, 1526–1532 (2011).

19. Fra, A. M., Williamson, E., Simons, K. & Parton, R. G. De novo formation of caveolae in lymphocytes by expression of VIP21-caveolin. *Proc. Natl Acad. Sci. USA* **92**, 8655–8659 (1995).
20. Li, S., Song, K. S., Koh, S. S., Kikuchi, A. & Lisanti, M. P. Baculovirus-based expression of mammalian caveolin in Sf21 insect cells: a model system for the biochemical and morphological study of caveolae biogenesis. *J. Biol. Chem.* **271**, 28647–28654 (1996).
21. Murata, M. et al. VIP21/caveolin is a cholesterol-binding protein. *Proc. Natl Acad. Sci. USA* **92**, 10339–10343 (1995).
22. Anderson, R. G. W., Kamen, B. A., Rothberg, K. G. & Lacey, S. W. Potocytosis: sequestration and transport of small molecules by caveolae. *Science* **255**, 410–411 (1992).
23. Parton, R. G. & Simons, K. The multiple faces of caveolae. *Nat. Rev. Mol. Cell Biol.* **8**, 185–194 (2007).
24. Couet, J., Sargiacomo, M. & Lisanti, M. P. Interaction of a receptor tyrosine kinase, EGF-R, with caveolins. Caveolin binding negatively regulates tyrosine and serine/threonine kinase activities. *J. Biol. Chem.* **272**, 30429–30438 (1997).
25. Song, K. S. et al. Co-purification and direct interaction of Ras with caveolin, an integral membrane protein of caveolae microdomains: detergent-free purification of caveolae membranes. *J. Biol. Chem.* **271**, 9690–9697 (1996).
26. Engelman, J. A. et al. Reciprocal regulation of Neu tyrosine kinase activity and caveolin-1 protein expression in vitro and in vivo: implications for human breast cancer. *J. Biol. Chem.* **273**, 20448–20455 (1998).
27. Zundel, W., Swiersz, L. M. & Giaccia, A. Caveolin 1-mediated regulation of receptor tyrosine kinase-associated phosphatidylinositol 3-kinase activity by ceramide. *Mol. Cell Biol.* **20**, 1507–1514 (2000).
28. Lo, H. P. et al. The caveolin-Cavin system plays a conserved and critical role in mechanoprotection of skeletal muscle. *J. Cell Biol.* **210**, 833–849 (2015).
29. Sinha, B. et al. Cells respond to mechanical stress by rapid disassembly of caveolae. *Cell* **144**, 402–413 (2011).
30. Cheng, J. P. X. et al. Caveolae protect endothelial cells from membrane rupture during increased cardiac output. *J. Cell Biol.* **211**, 53–61 (2015).
31. Lim, Y. W. et al. Caveolae protect notochord cells against catastrophic mechanical failure during development. *Curr. Biol.* **27**, 1968–1981.e7 (2017).
32. Garcia, J. et al. Sheath cell invasion and trans-differentiation repair mechanical damage caused by loss of caveolae in the zebrafish notochord. *Curr. Biol.* **27**, 1982–1989.e3 (2017).
33. Dewulf, M. et al. Dystrophy-associated caveolin-3 mutations reveal that caveolae couple IL6/STAT3 signaling with mechanosensing in human muscle cells. *Nat Commun* **10**, 1974 (2019).
34. Echarri, A. & del Pozo, M. A. Caveolae - mechanosensitive membrane invaginations linked to actin filaments. *J. Cell Sci.* **128**, 2747–2758 (2015).
35. Echarri, A. et al. Caveolar domain organization and trafficking is regulated by Abl kinases and mDia1. *J. Cell Sci.* **125**, 3097–3113 (2012).
36. Echarri, A. et al. An Abl-FBP17 mechanosensing system couples local plasma membrane curvature and stress fiber remodeling during mechanoadaptation. *Nat Commun* **10**, 5828 (2019).
37. Golani, G., Ariotti, N., Parton, R. G. & Kozlov, M. M. Membrane curvature and tension control the formation and collapse of caveolar superstructures. *Dev. Cell* **48**, 523–538.e4 (2019).
38. del Pozo, M. A. et al. Phospho-caveolin-1 mediates integrin-regulated membrane domain internalization. *Nat. Cell Biol.* **7**, 901–908 (2005).
39. Rothberg, K. G. et al. Caveolin, a protein component of caveolae membrane coats. *Cell* **68**, 673–682 (1992).
40. Parton, R. G., Molero, J. C., Floetenmeyer, M., Green, K. M. & James, D. E. Characterization of a distinct plasma membrane macrodomain in differentiated adipocytes. *J. Biol. Chem.* **277**, 46769–46778 (2002).
41. Bosch, M. et al. Caveolin-1 deficiency causes cholesterol-dependent mitochondrial dysfunction and apoptotic susceptibility. *Curr. Biol.* **21**, 681–686 (2011).
42. Pol, A. et al. A caveolin dominant negative mutant associates with lipid bodies and induces intracellular cholesterol imbalance. *J. Cell Biol.* **152**, 1057–1070 (2001).
43. Pol, A. et al. Dynamic and regulated association of caveolin with lipid bodies: modulation of lipid body motility and function by a dominant negative mutant. *Mol. Biol. Cell* **15**, 99–110 (2004).
44. Bosch, M., Mari, M., Gross, S. P., Fernández-Checa, J. C. & Pol, A. Mitochondrial cholesterol: a connection between caveolin, metabolism, and disease. *Traffic* **12**, 1483–1489 (2011).
45. Kim, C. A. et al. Association of a homozygous nonsense caveolin-1 mutation with berardinelli-seip congenital lipodystrophy. *J. Clin. Endocrinol. Metab.* **93**, 1129–1134 (2008).
46. Cao, H., Alston, L., Ruschman, J., & Hegele, R. A. Heterozygous CAV1 frameshift mutations (MIM 601047) in patients with atypical partial lipodystrophy and hypertriglyceridemia. *Lipids Health Dis.* **7**, 3 (2008).
47. Schrauwen, I. et al. A frame-shift mutation in CAV1 is associated with a severe neonatal progeroid and lipodystrophy syndrome. *PLoS ONE* **10**, e0131797 (2015).
48. Garg, A., Kircher, M., del Campo, M., Amato, R. S. & Agarwal, A. K. Whole exome sequencing identifies de novo heterozygous CAV1 mutations associated with a novel neonatal onset lipodystrophy syndrome. *Am. J. Med. Genet. A* **167**, 1796–1806 (2015).
49. Razani, B. et al. Caveolin-1-deficient mice are lean, resistant to diet-induced obesity, and show hypertriglyceridemia with adipocyte abnormalities. *J. Biol. Chem.* **277**, 8635–8647 (2002).
50. Martin, S. et al. Caveolin-1 deficiency leads to increased susceptibility to cell death and fibrosis in white adipose tissue: characterization of a lipodystrophic model. *PLoS ONE* **7**, 1–9 (2012).
51. Ardissonne, A. et al. Novel PTRF mutation in a child with mild myopathy and very mild congenital lipodystrophy. *BMC Med. Genet.* **14**, 1–5 (2013).
52. Hayashi, Y. K. et al. Human PTRF mutations cause secondary deficiency of caveolins resulting in muscular dystrophy with generalized lipodystrophy. *J. Clin. Investig.* **119**, 2623–2633 (2009).
53. Murakami, N. et al. Congenital generalized lipodystrophy type 4 with muscular dystrophy: Clinical and pathological manifestations in early childhood. *Neuromuscul. Disord.* **23**, 441–444 (2013).
54. Rajab, A. et al. Fatal cardiac arrhythmia and long-QT syndrome in a new form of congenital generalized lipodystrophy with muscle rippling (CGL4) due to PTRF-CAVIN mutations. *PLoS Genet.* **6**, e1000874 (2010).
55. Shastry, S. et al. Congenital generalized lipodystrophy, type 4 (CGL4) associated with myopathy due to novel PTRF mutations. *Am. J. Med. Genet. A* **152**, 2245–2253 (2010).
56. Jelani, M. et al. Novel nonsense mutation in the PTRF gene underlies congenital generalized lipodystrophy in a consanguineous Saudi family. *Eur. J. Med. Genet.* **58**, 216–221 (2015).
57. Akinci, G. et al. Spectrum of clinical manifestations in two young Turkish patients with congenital generalized lipodystrophy type 4. *Eur. J. Med. Genet.* **59**, 320–324 (2016).
58. Nilay Güneş et al. Congenital generalized lipodystrophy: the evaluation of clinical follow-up findings in a series of five patients with type 1 and two patients with type 4. *Eur. J. Med. Genet.* **63**, 2–7 (2019).
59. Patni, N., Vuitch, F. & Garg, A. Postmortem findings in a young man with congenital generalized lipodystrophy, type 4 due to CAVIN1 mutations. *J. Clin. Endocrinol. Metab.* **104**, 957–960 (2019).



60. Glenney, J. R. Tyrosine phosphorylation of a 22-kDa protein is correlated with transformation by Rous sarcoma virus. *J. Biol. Chem.* **264**, 20163–20166 (1989).
61. Glenney, J. R. & Zokas, L. Novel tyrosine kinase substrates from Rous sarcoma virus-transformed cells are present in the membrane skeleton. *J. Cell Biol.* **108**, 2401–2408 (1989).
62. Joshi, B. et al. Phosphorylated caveolin-1 regulates Rho/ROCK-dependent focal adhesion dynamics and tumor cell migration and invasion. *Cancer Res.* **68**, 8210–8220 (2008).
63. Goetz, J. G. et al. Concerted regulation of focal adhesion dynamics by galectin-3 and tyrosine-phosphorylated caveolin-1. *J. Cell Biol.* **180**, 1261–1275 (2008).
64. Grande-García, A. et al. Caveolin-1 regulates cell polarization and directional migration through Src kinase and Rho GTPases. *J. Cell Biol.* **177**, 683–694 (2007).
65. Mastick, C., Brady, M. & Saltiel, A. Insulin-stimulates the tyrosine phosphorylation of caveolin. *J. Cell Biol.* **129**, 1523–1531 (1995).
66. Mastick, C. C. & Saltiel, A. R. Insulin-stimulated tyrosine phosphorylation of caveolin is specific for the differentiated adipocyte phenotype in 3T3-L1 cells. *J. Biol. Chem.* **272**, 20706–20714 (1997).
67. Kim, Y. N., Wiepz, G. J., Guadarrama, A. G. & Bertics, P. J. Epidermal growth factor-stimulated tyrosine phosphorylation of caveolin-1. Enhanced caveolin-1 tyrosine phosphorylation following aberrant epidermal growth factor receptor status. *J. Biol. Chem.* **275**, 7481–7491 (2000).
68. Lee, H. et al. Constitutive and growth factor-regulated phosphorylation of caveolin-1 occurs at the same site (Tyr-14) in vivo: Identification of a c-Src/Cav-1/Grb7 signaling cassette. *Mol. Endocrinol.* **14**, 1750–1775 (2000).
69. Orlichenko, L., Huang, B., Krueger, E. & McNiven, M. A. Epithelial growth factor-induced phosphorylation of caveolin 1 at tyrosine 14 stimulates caveolae formation in epithelial cells. *J. Biol. Chem.* **281**, 4570–4579 (2006).
70. Volonté, D., Galbiati, F., Pestell, R. G. & Lisanti, M. P. Cellular stress induces the tyrosine phosphorylation of caveolin-1 (Tyr14) via activation of p38 mitogen-activated protein kinase and c-Src kinase. Evidence for caveolae, the actin cytoskeleton, and focal adhesions as mechanical sensors of osmotic stress. *J. Biol. Chem.* **276**, 8094–8103 (2001).
71. Pellegrinelli, V. et al. Human adipocyte function is impacted by mechanical cues. *J. Pathol.* **233**, 183–195 (2014).
72. Radcliff, C. & Rizzo, V. Integrin mechanotransduction stimulates caveolin-1 phosphorylation and recruitment of Csk to mediate actin reorganization. *Am. J. Physiol. Heart Circ. Physiol.* **288**, 936–945 (2005).
73. Joshi, B. et al. Phosphocaveolin-1 is a mechanotransducer that induces caveola biogenesis via Egr1 transcriptional regulation. *J. Cell Biol.* **199**, 425–435 (2012).
74. Zimnicka, A. M. et al. Src-dependent phosphorylation of caveolin-1 Tyr-14 promotes swelling and release of caveolae. *Mol. Biol. Cell* **27**, 2090–2106 (2016).
75. le Lay, S., Briand, N. & Dugail, I. Adipocyte size fluctuation, mechano-active lipid droplets and caveolae. *Adipocyte* **4**, 158–160 (2015).
76. Del Pozo, M. A., Lolo, F. N. & Echarri, A. Caveolae: mechanosensing and mechanotransduction devices linking membrane trafficking to mechanoadaptation. *Curr. Opin. Cell Biol.* **68**, 113–123 (2021).
77. Bundgaard, M., Hagman, P. & Crone, C. The three-dimensional organization of plasmalemmal vesicular profiles in the endothelium of rat heart capillaries. *Microvasc. Res.* **25**, 358–368 (1983).
78. Bundgaard, M., Frokjaer-Jensen, J. & Crone, C. Endothelial plasmalemmal vesicles as elements in a system of branching invaginations from the cell surface. *Proc. Natl Acad. Sci. USA* **76**, 6439–6442 (1979).
79. Popescu, L. M., Gherghiceanu, M., Mandache, E. & Cretoiu, D. Caveolae in smooth muscles: Nanocontacts. *J. Cell. Mol. Med.* **10**, 960–990 (2006).
80. Ring, A., le Lay, S., Pohl, J., Verkade, P. & Stremmel, W. Caveolin-1 is required for fatty acid translocase (FAT/CD36) localization and function at the plasma membrane of mouse embryonic fibroblasts. *Biochim. Biophys. Acta Mol. Cell Biol. Lipids* **1761**, 416–423 (2006).
81. Matthaues, C. et al. EHD2-mediated restriction of caveolar dynamics regulates cellular fatty acid uptake. *Proc. Natl Acad. Sci. USA* **117**, 7471–7481 (2020).
82. Muir, L. A. et al. Adipose tissue fibrosis, hypertrophy, and hyperplasia: correlations with diabetes in human obesity. *Obesity* **24**, 597–605 (2016).
83. Divoux, A. et al. Fibrosis in human adipose tissue: composition, distribution, and link with lipid metabolism and fat mass loss. *Diabetes* **59**, 2817–2825 (2010).
84. Zwick, R. K., Guerrero-Juarez, C. F., Horsley, V. & Plikus, M. V. Anatomical, physiological, and functional diversity of adipose tissue. *Cell Metab.* **27**, 68–83 (2018).
85. Strålfors, P. Autolysis of isolated adipocytes by endogenously produced fatty acids. *FEBS Lett.* **263**, 153–154 (1990).
86. Mathieson, P. W., Wuirzner, R., Oliveira, D. B. G., Lachmann, P. J. & Peters, D. K. Complement-mediated adipocyte lysis by nephritic factor sera. *J. Exp. Med.* **177**, 1827–1831 (1993).
87. Abbott, R. D. et al. Long term perfusion system supporting adipogenesis. *Methods* **84**, 84–89 (2015).
88. Haghiaci, M. et al. Increased death of adipose cells, a path to release cell-free DNA into systemic circulation of obese women. *Obesity* **20**, 2213–2219 (2012).
89. Lappas, M., Permezel, M. & Rice, G. E. Release of proinflammatory cytokines and 8-isoprostane from placenta, adipose tissue, and skeletal muscle from normal pregnant women and women with gestational diabetes mellitus. *J. Clin. Endocrinol. Metab.* **89**, 5627–5633 (2004).
90. Moreno-Navarrete, J. M. et al. OCT1 expression in adipocytes could contribute to increased metformin action in obese subjects. *Diabetes* **60**, 168–176 (2011).
91. Garcia, R. Nanomechanical mapping of soft materials with the atomic force microscope: Methods, theory and applications. *Chem. Soc. Rev.* **49**, 5850–5884 (2020).
92. Colom, A. et al. A fluorescent membrane tension probe. *Nat. Chem.* **10**, 1118–1125 (2018).
93. Lolo, F. N. et al. Caveolin-1 dolines form a distinct and rapid caveolae-independent mechanoadaptation system. *Nat. Cell Biol.* **25**, 120–133 (2023).
94. Buwa, N., Mazumdar, D. & Balasubramanian, N. Caveolin1 tyrosine-14 phosphorylation: role in cellular responsiveness to mechanical cues. *J. Membr. Biol.* **253**, 509–534 (2020).
95. Kassan, A. et al. Acyl-CoA synthetase 3 promotes lipid droplet biogenesis in ER microdomains. *J. Cell Biol.* **203**, 985–1001 (2013).
96. Bersuker, K. et al. A proximity labeling strategy provides insights into the composition and dynamics of lipid droplet proteomes. *Dev. Cell* **44**, 97–112.e7 (2018).
97. Morén, B. et al. EHD2 regulates adipocyte function and is enriched at cell surface-associated lipid droplets in primary human adipocytes. *Mol. Biol. Cell* **30**, 1147–1159 (2019).
98. Lachowski, D. et al. Substrate stiffness-driven membrane tension modulates vesicular trafficking via caveolin-1. *ACS Nano* **16**, 4322–4337 (2022).
99. Stout, J. G. & Kirley, T. L. Control of cell membrane ecto-ATPase by oligomerization state: intermolecular cross-linking modulates ATPase activity. *Biochemistry* **35**, 8289–8298 (1996).
100. Park, D. S. et al. Caveolin-1 null (-/-) mice show dramatic reductions in life span. *Biochemistry* **42**, 15124–15131 (2003).

101. Frank, P. G. et al. Genetic ablation of caveolin-1 confers protection against atherosclerosis. *Arterioscler. Thromb. Vasc. Biol.* **24**, 98–105 (2004).
102. Frank, P. G., Pavlides, S., Cheung, M. W. C., Daumer, K. & Lisanti, M. P. Role of caveolin-1 in the regulation of lipoprotein metabolism. *Am. J. Physiol. Cell Physiol.* **295**, C242 (2008).
103. Shoham, N. et al. Adipocyte stiffness increases with accumulation of lipid droplets. *Biophys. J.* **106**, 1421–1431 (2014).
104. Gervásio, O. L., Phillips, W. D., Cole, L. & Allen, D. G. Caveolae respond to cell stretch and contribute to stretch-induced signaling. *J. Cell Sci.* **124**, 3581–3590 (2011).
105. Han, B. et al. Characterization of a caveolin-1 mutation associated with both pulmonary arterial hypertension and congenital generalized lipodystrophy. *Traffic* **17**, 1297–1312 (2016).
106. de Haan, W. Lipodystrophy and muscular dystrophy caused by PTRF mutations. *Clin. Genet.* **77**, 436–437 (2010).
107. Dwianingsih, E. K. et al. A Japanese child with asymptomatic elevation of serum creatine kinase shows PTRF-CAVIN mutation matching with congenital generalized lipodystrophy type 4. *Mol. Genet. Metab.* **101**, 233–237 (2010).
108. Hubert, M. et al. Lipid accumulation controls the balance between surface connection and scission of caveolae. *Elife* **9**, 1–31 (2020).
109. Parton, R. G. & del Pozo, M. A. Caveolae as plasma membrane sensors, protectors and organizers. *Nat. Rev. Mol. Cell Biol.* **14**, 98–112 (2013).
110. Le Lay, S. et al. Cholesterol-induced caveolin targeting to lipid droplets in adipocytes: A role for caveolar endocytosis. *Traffic* **7**, 549–561 (2006).
111. Zhang, Y. et al. SWELL1 is a regulator of adipocyte size, insulin signalling and glucose homeostasis. *Nat. Cell Biol.* **19**, 504–517 (2017).
112. Parton, R. G., Taraska, J. W. & Lundmark, R. Is endocytosis by caveolae dependent on dynamin? *Nat. Rev. Mol. Cell Biol.* **25**, 511–512 (2024).
113. Raucher, D. & Sheetz, M. P. Membrane expansion increases endocytosis rate during mitosis. *J. Cell Biol.* **144**, 497–506 (1999).
114. Dai, J., Ping Ting-Beall, H. & Sheetz, M. P. The secretion-coupled endocytosis correlates with membrane tension changes in RBL 2H3 cells. *J. Gen. Physiol.* **110**, 1–10 (1997).
115. Wu, X. S. et al. Membrane tension inhibits rapid and slow endocytosis in secretory cells. *Biophys. J.* **113**, 2406–2414 (2017).
116. Drab, M. et al. Loss of caveolae, vascular dysfunction, and pulmonary defects in caveolin-1 gene-disrupted mice. *Science* **293**, 2449–2452 (2001).
117. Folgueira, C. et al. Hypothalamic dopamine signalling regulates brown fat thermogenesis. *Nat. Metab.* **1**, 811–829 (2019).
118. Moreno-Vicente, R. et al. Caveolin-1 modulates mechanotransduction responses to substrate stiffness through actin-dependent control of YAP. *Cell Rep.* **25**, 1622–1635.e6 (2018).
119. Baecker, V., Lacroix, M. & Cavalier, P. *MRI Adipocyte Tools* (2012).
120. Schindelin, J. et al. Fiji: an open-source platform for biological-image analysis. *Nat. Methods* **9**, 676–682 (2012).
121. Legland, D., Arganda-Carreras, I. & Andrey, P. MorphoLibJ: integrated library and plugins for mathematical morphology with ImageJ. *Bioinformatics* **32**, btw413 (2016).
122. Sobel, I., & Feldman, G. A 3×3 isotropic gradient operator for image processing. in *a talk at the Stanford Artificial Project in* 271–272 (1968).
123. Meyer, F. & Beucher, S. Morphological segmentation. *J. Vis. Commun. Image Represent* **1**, 21–46 (1990).
124. Thévenaz, P. & Unser, M. User-friendly semiautomated assembly of accurate image mosaics in microscopy. *Microsc. Res. Tech.* **70**, 135–146 (2007).
125. Preibisch, S., Saalfeld, S. & Tomancak, P. Globally optimal stitching of tiled 3D microscopic image acquisitions. *Bioinformatics* **25**, 1463–1465 (2009).
126. Kurt De Vos. *Cell Counter* (2001).
127. Kirkham, M. et al. Ultrastructural identification of uncoated caveolin-independent early endocytic vehicles. *J. Cell Biol.* **168**, 465–476 (2005).
128. R Core Team. *R: A Language And Environment For Statistical Computing* (2017).
129. Digman, M. A., Caiolfa, V. R., Zamai, M. & Gratton, E. The phasor approach to fluorescence lifetime imaging analysis. *Biophys. J.* **94**, L14–6 (2008).
130. Hayer, A., Stoeber, M., Bissig, C. & Helenius, A. Biogenesis of caveolae: stepwise assembly of large caveolin and cavin complexes. *Traffic* **11**, 361–382 (2010).
131. Sage, D., Neumann, F. R., Hediger, F., Gasser, S. M. & Unser, M. Automatic tracking of individual fluorescence particles: application to the study of chromosome dynamics. *IEEE Trans. Image Process* **14**, 1372–1383 (2005).
132. RStudio Team. *RStudio: Integrated Development for R* (2020).
133. Sarkar, D. *Lattice: Multivariate Data Visualization with R* (2008).
134. Wickham, H. *ggplot2: Elegant Graphics for Data Analysis* (2009).
135. Eklund, A. *Beeswarm: The Bee Swarm Plot, an Alternative to Stripchart*. R package version 0.2.3. (2016).
136. Wickham, H. *Split-Apply-Comb. Strategy Data Anal.* **40**, 1–29 (2011).
137. Matt D. & Arun S. data.table: extension of ‘data.frame’. *R package version 1.12.0* (2019).
138. Therneau, T. *A Package for Survival Analysis in S* (2015).
139. Terry, M. T. & Patricia, M. G. *Modeling Survival Data: Extending the Cox Model*. (Springer, 2000).
140. Kassambara, A. *survminer: Drawing Survival Curves using ‘ggplot2’* (2019).
141. Dinno, A. *dunn.test: Dunn’s Test of Multiple Comparisons Using Rank Sums* (2017).
142. Ogle, D. H., Wheeler, P. & Dinno, A. *FSA: Fisheries Stock Analysis* (2023).
143. Garcia, P. D. & Garcia, R. Determination of the elastic moduli of a single cell cultured on a rigid support by force microscopy. *Biophys. J.* **114**, 2923–2932 (2018).

## Acknowledgements

We thank Teresa Osteso and Sarah Francoz for technical support; the Transgenesis and Pluripotent Cell Technology Units at CNIC (in particular Drs. Giovanna Giovino and Luis Miguel Criado) for their support in animal model generation; Juan José Lazcano and Elisabet Daniel for mouse colony management; the Microscopy Unit of CNIC (in particular, Verónica Labrador, Elvira Arza and Hélio Duarte) for technical support and guidance; the Histopathology Unit of CNIC, and Antonio de Molina in particular, for sample processing, staining and guidance. Francisco Urbano and Covadonga Díaz from Universidad Autónoma de Madrid for TEM technical support; Milagros Guerra, Tania Matamoros, and María Teresa Rojas, from Centro de Biología Molecular Severo Ochoa (CBMSO), for technical support in immunogold experiments; and Stuart Pocock for advice in statistical analysis. This study was supported by grants from the Spanish Ministry of Science and Innovation (MICIIN)/ Agencia Estatal de Investigación (AEI)/European Regional Development Fund (ARDF/FEDER) “A way to make Europe” (SAF2017-83130-R, IGP-SO grant MINSEV1512-07-2016, BFU2016-81912-REDC, and SAF2020 (PID2020-118658RB-I00)), Comunidad Autónoma de Madrid (Tec4Bio-CM, S2018/NMT-4443), Fundació La Marató de TV3 (201936-30-31), Asociación Española Contra el Cáncer (PROYE20089DELP), and Fundación Obra Social La Caixa (AtheroConvergence, HR20-00075), all to M.A.d.P. M.C.M.A-P. was sponsored by a *la Caixa-Severo Ochoa* international doctoral fellowship, 2015 call. V.J.-J. was ECR trainee of a Horizon 2020 MSCA-ITN (BIOPOL, 641639), of which M.A.d.P. was co-awardee. M.S.-A. is funded by the Ramón y Cajal program (RYC2020-029690) and is recipient of a MICINN Grant (PID2021-128106NA-I00). G.S.: MINECO-PID2019-104399RB-I00, Fundación Jesús Serra, EFSO/

Lilly European Diabetes Research Programme. Optical microscopy experiments were performed using the appliances of the Microscopy and Dynamic Unit at CNIC, ICTS-ReDib, sponsored by MCIN/AEI/10.13039/501100011033. The CNIC is supported by the Instituto de Salud Carlos III (ISCIII), the Ministerio de Ciencia, Innovación y Universidades (MICIU) and the Pro CNIC Foundation, and is a Severo Ochoa Center of Excellence (grant CEX2020-001041-S funded by MICIU/AEI/10.13039/501100011033).

## Author contributions

M.A.d.P conceived the project, supervised procedures and experimental design and edited the manuscript. M.C.M.A-P. designed and performed experiments, analyzed results, and drafted the manuscript. M.G. and A.C. generated the new Y14F/Y14F mouse model. M.G. performed initial HFD and AFM experiments. C.G. and R.G. performed AFM measurements. M.C., M. T., S.T., and D.P. provided technical assistance and support in manual caveolae segmentation and adipocyte image analysis. V.J.-J. and D.J.C. guided automated image analysis. M.Z. performed FLIM measurements of Flipper-TR and with assistance of M.T. performed image analysis and quantification. M.S.-A., F-N.L., and A.E. edited the manuscript, contributed to experimental design, and performed in vitro experiments. C.F. and R.N. performed food intake, energy expenditure, respiratory quotient, and locomotor activity experiments. G.S. performed glucose tolerance test and insulin tolerance test experiments.

## Competing interests

The authors declare no competing interests.

## Additional information

**Supplementary information** The online version contains supplementary material available at <https://doi.org/10.1038/s41467-024-54224-y>.

**Correspondence** and requests for materials should be addressed to Miguel A. Del Pozo.

**Peer review information** *Nature Communications* thanks the anonymous reviewer(s) for their contribution to the peer review of this work. A peer review file is available.

**Reprints and permissions information** is available at <http://www.nature.com/reprints>

**Publisher's note** Springer Nature remains neutral with regard to jurisdictional claims in published maps and institutional affiliations.

**Open Access** This article is licensed under a Creative Commons Attribution-NonCommercial-NoDerivatives 4.0 International License, which permits any non-commercial use, sharing, distribution and reproduction in any medium or format, as long as you give appropriate credit to the original author(s) and the source, provide a link to the Creative Commons licence, and indicate if you modified the licensed material. You do not have permission under this licence to share adapted material derived from this article or parts of it. The images or other third party material in this article are included in the article's Creative Commons licence, unless indicated otherwise in a credit line to the material. If material is not included in the article's Creative Commons licence and your intended use is not permitted by statutory regulation or exceeds the permitted use, you will need to obtain permission directly from the copyright holder. To view a copy of this licence, visit <http://creativecommons.org/licenses/by-nc-nd/4.0/>.

© The Author(s) 2024

<sup>1</sup>Mechanoadaptation and Caveolae Biology lab, Novel mechanisms in atherosclerosis program. Centro Nacional de Investigaciones Cardiovasculares (CNIC), Madrid, Spain. <sup>2</sup>ForceTool group, Instituto de Ciencia de Materiales de Madrid (ICMM), CSIC, Madrid, Spain. <sup>3</sup>Cellomics Unit, Cell and Developmental Biology Area. Centro Nacional de Investigaciones Cardiovasculares (CNIC), Madrid, Spain. <sup>4</sup>Microscopy and Dynamic Imaging Unit, Centro Nacional de Investigaciones Cardiovasculares (CNIC), Madrid, Spain. <sup>5</sup>Centro de Investigación en Medicina Molecular y Enfermedades Crónicas CIMUS, Santiago de Compostela, Spain. <sup>6</sup>Stress kinases in Diabetes, Cancer and Cardiovascular Disease lab. Cardiovascular risk factors & brain function program, Centro Nacional de Investigaciones Cardiovasculares (CNIC), Madrid, Spain. <sup>7</sup>Cell Compartmentalization, Homeostasis and Inflammation lab, Department of Metabolic and Inflammatory Diseases. Instituto de Investigaciones Biomédicas "Sols-Morreale"-CSIC, Madrid, Spain. <sup>8</sup>Mechanobiology of Organelles lab. Department of Cellular and Molecular Biology. Centro de Investigaciones Biológicas Margarita Salas – CSIC, Madrid, Spain. <sup>9</sup>Present address: Department of Science and Agroforestry Technology and Genetics, Faculty of Biochemistry and Environmental Sciences, University of Castilla-La Mancha, Toledo, Spain. <sup>10</sup>Present address: Allergy Therapeutics, Avenida Punto Es, 12, 28805 Alcalá de Henares, Madrid, Spain. <sup>11</sup>Present address: Department of Health Science, Universidad Católica Santa Teresa de Jesús de Ávila, Ávila, Spain. <sup>12</sup>Present address: Stress kinases in Diabetes, Cancer and Cardiovascular Disease lab. Cardiovascular risk factors & brain function program, Centro Nacional de Investigaciones Cardiovasculares (CNIC), Madrid, Spain. <sup>13</sup>Present address: Department of Molecular Pharmacology, Lilly Research Laboratories, Alcobendas, Spain. <sup>14</sup>Present address: Centro Nacional de Investigaciones Oncológicas (CNIO), Madrid, Spain. <sup>15</sup>These authors contributed equally: Mauro Català-Montoro, Mónica Toledano-Donado, Sara Terrés-Domínguez, Dácil M. Pavón.

✉ e-mail: [madelpozo@cnic.es](mailto:madelpozo@cnic.es)